RESERVOIR COMPUTING MODEL USING A SINGLE NONLINEAR NANOELECTROMECHANICAL RESONATOR AT ATMOSPHERIC CONDITIONS

A THESIS SUBMITTED TO

THE GRADUATE SCHOOL OF ENGINEERING AND SCIENCE

OF BILKENT UNIVERSITY

IN PARTIAL FULFILLMENT OF THE REQUIREMENTS FOR

THE DEGREE OF

MASTER OF SCIENCE

IN

MECHANICAL ENGINEERING

By

Enise Kartal

July 2024

RESERVOIR COMPUTING MODEL USING A SINGLE NON-LINEAR NANOELECTROMECHANICAL RESONATOR AT ATMOSPHERIC CONDITIONS
By Enise Kartal
July 2024

We certify that we have read this thesis and that in our opinion it is fully adequate, in scope and in quality, as a thesis for the degree of Master of Science.

Mehmet Selim Hanay (Advisor)

Alper Demir

Emine Yegân Erdem

Approved for the Graduate School of Engineering and Science:

Orhan Arıkan
Director of the Graduate School

ABSTRACT

RESERVOIR COMPUTING MODEL USING A SINGLE NONLINEAR NANOELECTROMECHANICAL RESONATOR AT ATMOSPHERIC CONDITIONS

Enise Kartal
M.S. in Mechanical Engineering
Advisor: Mehmet Selim Hanay
July 2024

Reservoir computing is an alternative method to conventional systems using computationally expensive recurrent neural networks (RNNs). In this method, the training is performed only at the final layer of a nonlinear physical system functioning as a black box substituted instead of the hidden layers in RNNs requiring intensive training. This study suggests using a small nanoelectromechanical systems (NEMS) resonator with intrinsic nonlinearities for reservoir computing instead of relying on complicated feedback loops or spatially extended reservoirs as used in the earlier works. The linear classification is made possible by transforming the input data into a higher dimensional space, which is accomplished by utilizing the combination of the nonlinearity of the NEMS resonator and its fading memory behavior stemming from its transient response. Compared to reservoir computing using micromechanical resonators, the use of nanoelectromechanical resonators results in faster information processing, enabled by their rapid decay times arising from their small dimensions. Moreover, the implementation of the proposed NEMS reservoir computing architecture is more practical since it can operate at atmospheric conditions and occupies less space than its MEMS counterparts. This study emphasizes the efficient and feasible information processing potential of the suggested approach for a range of applications by the evaluation of its performance with the MNIST handwritten digit recognition task.

Keywords: Reservoir computing, physical neural networks, information processing, nonlinear dynamics, NEMS, fading memory, digit recognition.

ÖZET

ATMOSFERİK KOŞULLARDA TEK BİR DOĞRUSAL OLMAYAN NANOELEKTROMEKANİK REZONATÖR KULLANAN REZERVUAR HESAPLAMA MODELİ

Enise Kartal
Makine Mühendisliği, Yüksek Lisans
Tez Danışmanı: Mehmet Selim Hanay
Temmuz 2024

Rezervuar hesaplama, hesaplama açısından pahalı tekrarlayan nöral ağlarını (RNN'ler) kullanan geleneksel sistemlere alternatif bir yöntemdir. Bu yöntemde eğitim, yoğun eğitim gerektiren RNN'lerde gizli katmanların yerine kara kutu işlevi gören doğrusal olmayan bir fiziksel sistemin yalnızca son katmanında gerçekleştirilir. Bu çalışma, daha önceki çalışmalarda kullanıldığı gibi karmaşık geri besleme döngülerine veya uzaysal olarak genişletilmiş rezervuarlara güvenmek yerine, rezervuar hesaplaması için içsel doğrusal olmayan özelliklere sahip küçük bir nanoelektromekanik sistem (NEMS) rezonatörünün kullanılmasını önermektedir. Doğrusal sınıflandırma, giriş verilerinin daha yüksek boyutlu bir uzaya dönüştürülmesiyle mümkün kılınır; bu, NEMS rezonatörünün doğrusal olmama özelliğinin ve geçici yanıtından kaynaklanan sönümlenen bellek davranışının birleşimi kullanılarak gerçekleştirilir. Mikromekanik rezonatörlerin kullanıldığı rezervuar hesaplamayla karşılaştırıldığında, nanoelektromekanik rezonatörlerin kullanımı, küçük boyutlarından kaynaklanan hızlı bozulma süreleri sayesinde daha hızlı bilgi işlemeyle sonuçlanır. Ayrıca, önerilen NEMS rezervuar hesaplama mimarisinin uygulanması, atmosferik koşullarda çalışabilmesi ve MEMS muadillerine göre daha az yer kaplaması nedeniyle daha pratiktir. Bu çalışma, MNIST el yazısı rakam tanıma görevi ile performansının değerlendirilmesi yoluyla, bir dizi uygulama için önerilen yaklaşımın verimli ve uygulanabilir bilgi işleme potansiyelini vurgulamaktadır.

Anahtar sözcükler: Rezervuar hesaplama, fiziksel nöral ağlar, bilgi işleme, doğrusal olmayan dinamikler, NEMS, sönümlenen bellek, rakam tanıma.

Acknowledgement

I want to start my acknowledgments by thanking my advisor, Prof. M. Selim Hanay, whose contributions will always be unforgettable for me throughout my life. Not only because he is a brilliant advisor and a teacher but also because of his great personality, his kindness and understanding towards his students, and the excitement he conveys to the people while teaching inside or outside the classroom; he became the person I aimed to be if I could be a teacher one day. The mechatronics course I took from him when I was in my third year of undergraduate education, although most of it was online due to the pandemic, excited me so much and helped me to plan my career path. I am delighted and proud to have been able to work with him since then.

I express my gratitude to Prof. Emine Yegân Erden and Prof. Alper Demir for kindly accepting to be on my thesis committee and for providing me with their valuable comments on my thesis.

I thank all of our departmental and non-departmental professors for the invaluable lessons they taught. Also, I am deeply grateful to our department secretary, Ela Baycan, for kindly helping me in every regard during my eight years in Bilkent.

I want to thank my beloved partner, Doğa, for the invaluable support and love he gave me during the last year of my Master's degree, which is the most challenging and stressful one. His presence provided me peace and comfort throughout this time. I cannot even imagine how I could have stayed this strong without him. Thank goodness I have you, my love.

I want to express my endless gratitude to my high school friends Aybüke, Pınar, Ebru, and my primary school friend Gülşah for their endless support in every situation and for being the best sisters in the world rather than just friends. Without you, both my psychological well-being and my overall existence would be in less favorable situations.

Batu and Mohammed, thank you so much for teaching me the majority of knowledge I learned during my Master's degree and transforming hours of tedious work into enjoyable experiences. Your guidance has been essential for my improvement. Our friendship means a lot to me as well.

My dear housemates Senem and Güneş, I cannot thank you enough for giving me a real home experience during this stressful and chaotic period. We moved into the same house before we even met each other, and we got along and spent time together so well that it couldn't have been better. I will always remember and appreciate our 1.5 years together.

Aybars, İsmet, Harun, and Arda, who have shared their true friendship with me since my undergraduate years, thank you very much for all the fun times we spent together. Although everyone is working on different things in different places, I am proud of us for being able to meet regularly, even if not often.

My dear cousins Serra and İrem, you made me very happy when you came to Ankara to study. Your presence has provided me with the comforting familiarity of my childhood in this city. Thank you very much for the good times we spent together.

Many thanks to my friends from the graduate office, Özgür, Aykut, Emirhan, Ahmet, and Yusuf, for making working in the office fun. Without you, the office would be very boring, and we would not be able to handle so much work.

I thank the Hanay group members, Hashim, Uzay, Salehin, Ceren, Mehmet, and Burak, who helped me greatly in the laboratory work.

I also want to thank Dr. Cenk Yanik for his meticulous efforts on the electron beam lithography step of the fabrication of our devices.

Last but not least, I would like to express my profound gratitude and sincere appreciation to my family. Their trust and support in me is absolutely irreplaceable. Nothing else in the world can give me the happiness of having a family that loves me deeply, having a brother and cousins who take me as an example; and the pride I feel when my elders acknowledge that they have gained a greater understanding of the significance of education as a result of my diligent efforts. I will do my best not to disappoint them and to enhance their pride in me even more.

Contents

List of Figures

List of Tables

Chapter 1

Introduction

This thesis introduces a novel reservoir computing model developed with nanoelectromechanical systems (NEMS) using a single nonlinear nanoelectromechanical resonator under atmospheric conditions. Reservoir computing with nanoelectromechanical resonators is faster owing to their low ring-down times and is more portable and integrable due to their compact size and operation under ambient pressure. This chapter briefly mentions the reservoir computing background and applications, and then the motivation of the thesis for using nanoelectromechanical resonators within a reservoir computing system is presented.

1.1 Reservoir Computing

The development of increasingly complex algorithms and data processing tasks challenged conventional computational methods such as Recurrent Neural Networks (RNNs). In theory, RNNs are highly effective tools for addressing complicated temporal machine learning challenges [1]. However, numerous factors still prevent the widespread use of RNNs in real-world scenarios, such as the slow convergence rates restricting their practicality [2] and the need for high computing power to train deep neural networks. Thus, when a real-time training algorithm is needed for miniaturized devices working on low power, it is necessary to use an algorithm with reduced power consumption. These devices have limitations in terms of processing power, memory, and battery life, affecting the complexity of algorithms that can be implemented. Therefore, an efficient data analysis algorithm must be processed on-device to facilitate edge computation within large networks using these devices.

Reservoir computing (RC) technology was developed as an alternative to the mentioned challenging methods [1–3]. It operates as a reservoir of nonlinear elements to map input data into a high-dimensional space instead of working based on computationally expensive training processes as in RNNs [4]. Figure 1.1 illustrates the reservoir computing examples in biological organisms, digital systems, and physical systems. The mapping process entitles the reservoir computation as an inherent and efficient method and enables it to be used in resource-restricted edge devices for data analysis on-device, intending to achieve compact sensor sizes and low power consumption [5].

In recent works, different reservoir computing algorithms have been demonstrated. Earlier works established the RC field by defining nonlinear reservoirs implementing software in conventional digital systems, e.g., Echo State Networks (ESNs) [2] and Liquid State Machines (LSMs) [3]. The latest applications have been exploring nonlinear physical systems to be employed as rich reservoirs that can enhance the performance of the architecture [6, 7]. One application of RC in spoken word recognition employed a delay-coupled feedback loop to create virtual nodes in time using nonlinear MEMS resonators. A more recent work used the nonlinear MEMS resonators without delay-unit as an RC algorithm and carried out a variety of recognition tasks [8].

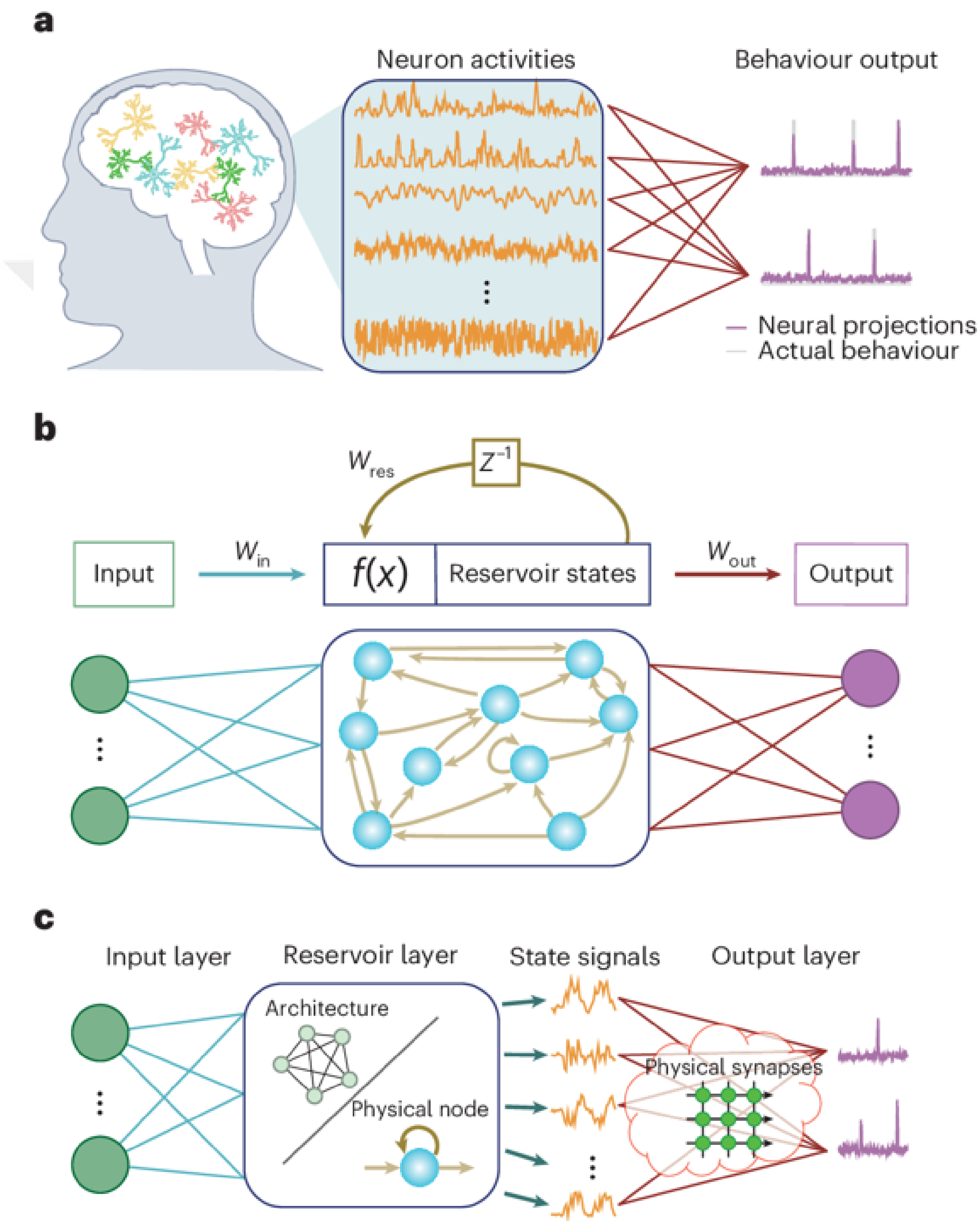

Figure 1.1: Biological, digital and physical reservoir computing examples, adapted from [4]

The working mechanism of reservoir computing can be summarized in three parts. Firstly, the nonlinear activation functions generated within the reservoir establish nonlinear relationships between the virtual nodes formed. These functions result in complex patterns that cannot be obtained using linear relationships. Moreover, this nonlinearity provides network connectivity within the reservoir, causing the virtual nodes to be interconnected in a complex web. The interaction between the nodes induces an inherent feedback loop, resulting in a rich representation of the states. Lastly, the reservoir dynamics operate by establishing connections between the past and current nodes, thus generating a memory. The connection between the nodes might be either spatial or temporal. Given the temporal connectivity of the nodes within the NEMS reservoir in this study, the past nodes refer to the nodes from previous time steps. The number of connected past nodes increases as the reservoir dynamics become more transient. As a result, the generated memory is a temporal memory, quantified with the ratio of the ring-down time of the resonator to the separation time between consecutive time steps.

The reservoir with the mentioned specifications processes the data and maps it into a higher dimensional space, implying the addition of more features and characteristics to the data representation. The single nonlinear NEMS resonator employed in this study functions as the reservoir in the above explanations. It takes input data and processes the data in its transient nonlinear dynamics to mimic neural network algorithms required for classification and forecasting tasks. The purpose of integrating NEMS in a reservoir computing system is to explore its reservoir computing capabilities and develop a faster and less power-consuming alternative to the computational neural network methods without necessarily striving for greater classification accuracies than theirs. The smallest physical reservoir computing example integrating mechanical systems utilized MEMS devices, which means that there is no reservoir computing example utilizing NEMS in the literature.

There are significant distinctions between performing reservoir computing using MEMS and NEMS. NEMS devices are three order-of-magnitude smaller than MEMS devices, meaning that their operating frequencies are three order-of-magnitude higher; thus, they are much faster. Since the aim of physical reservoir computing is to perform real-time data processing on-device with reduced power and storage consumption, NEMS devices are more suited for this purpose compared to MEMS devices. In addition to these advantages of NEMS over MEMS, the NEMS in this study is utilized under atmospheric conditions, creating another crucial difference from the other mechanical reservoir computing applications, eliminating the need for complex vacuum systems. As an exemplary comparison, the MEMS used in the reservoir computing system in [8] is operated under vacuum, with two thousand times larger dimensions than the NEMS used in this study. Also, the ring-down time of the MEMS ranges from 16 to 35 ms, which is four thousand times slower than the NEMS.

Therefore, this study stands apart from its counterparts for multiple reasons, rendering it a novel application. This study is the first to employ NEMS in this particular system, aiming to address a benchmark problem as a starting point.

1.2 Motivation

The works mentioned in the previous section have been the motivation for the RC with NEMS project, aiming for small, low-power consuming sensors with intrinsic reservoir characteristics. The employment of NEMS in RC applications offers smaller occupations in miniaturized sensors, leading to less footprint than using larger sensors. As a result of their operation at the nanoscale, NEMS has a lower power consumption. Owing to their compact size, their operation speed is higher than that of their MEMS equivalents, offering an effective reservoir with computational advantages that can perform real-time, on-device data processing.

It is essential for RC to have a high representation capability in order to make the system more efficient, and typical time-delayed RC relies on a large number of parameter optimizations for this purpose. Another crucial aspect of the application of RC is the feeding of the input and the mapping of it into higher dimensions through the use of the mask function. Previous works claimed that this step is carried out through a self-masking procedure within the reservoir, which operates on a feedback-loop basis [8]. An artificial fading memory is created by modulating the input signal and feeding the response of the reservoir back to the system through this masking procedure, which requires challenging hyperparameter optimizations. In order to eliminate these exhausting optimization steps, a similar concept is used in this work, investigating the memory capabilities of NEMS rather than making use of a mask function. This critical distinction motivated this work towards research on the intrinsic nonlinearities and fading memory of the NEMS-based RC systems.

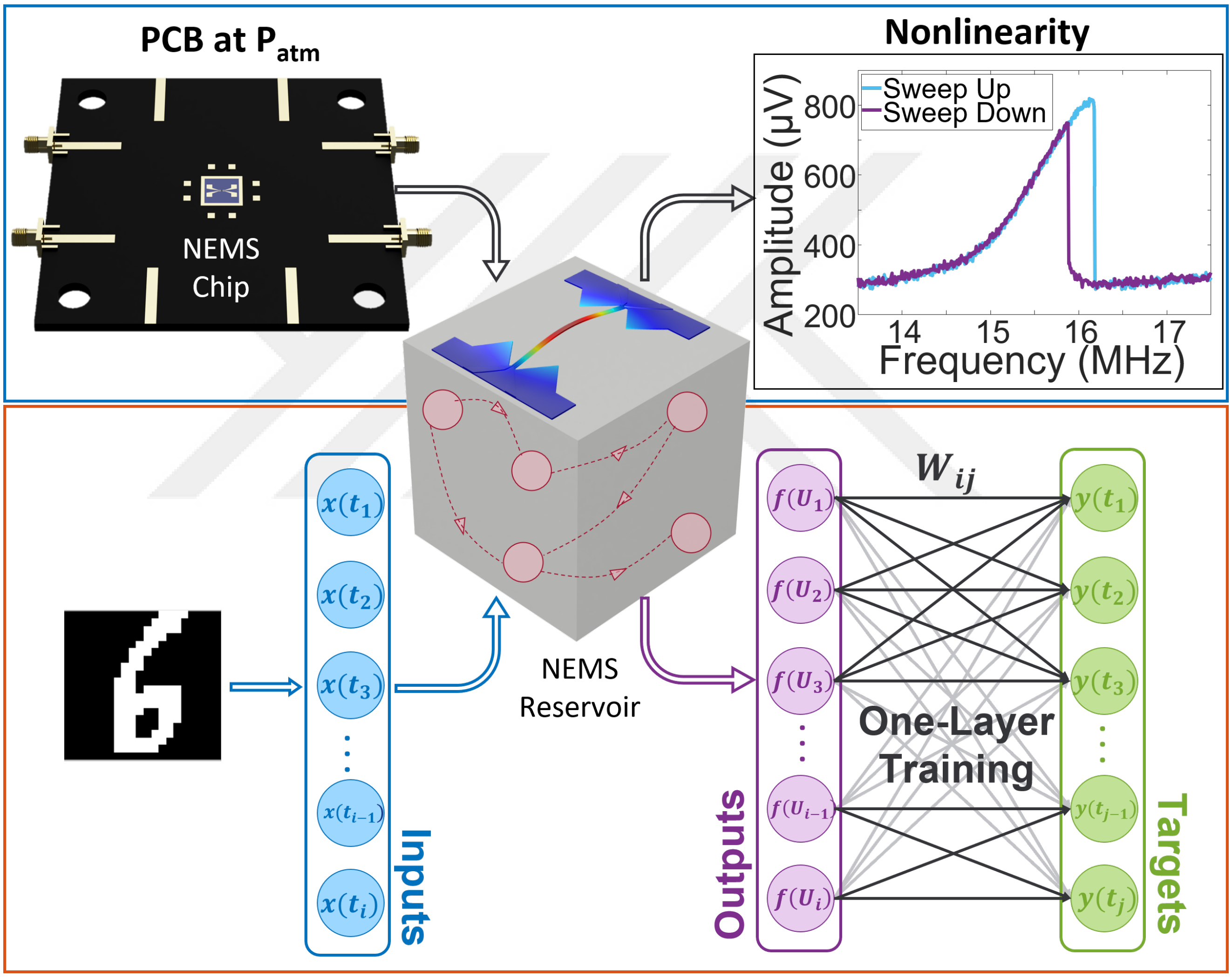

Figure 1.2: Reservoir computing architecture with NEMS at ambient pressure. Schematic of the nonlinear nanomechanical resonator-based reservoir computing system. The targets are the linear weighted sums of the output nodes of the reservoir. The nodes in the reservoir are the virtual nodes created by the nonlinearity of NEMS.

The proposed architecture contains three main parts: the input layer, the reservoir (a single NEMS resonator), and the output layer. Since the NEMS reservoir works with vectorized data, the input signal is initially vectorized, normalized, and preprocessed before being fed to the reservoir. Then, this signal is subjected to amplitude modulation with another signal that possesses the nonlinear response amplitude of the resonator at its fundamental mode. The information processing within the reservoir occurs owing to this modulation step, combining the input data and the nonlinear dynamics of the system, leading to the linear separability of different classes through the mapping of the input into a high-dimensional space. Along with this nonlinearity, the separation time between the sample points of the input data has been maintained below the ring-down time of the resonator to keep it at its transient regime. Due to this transient response, the previous and current input values are combined within the reservoir, enhancing its memory characteristics and resulting in the fading memory property of the NEMS reservoir. Consequently, the reservoir output is collected and utilized in training algorithms that function with linear regression. Figure 1.2 illustrates the explained architecture.

The ring-down time observed in this work is distinguished from its counterparts with a value of $6.25\mu s$. Another RC system with no delayed feedback loop was published recently [8], with relatively higher ring-down times, from 16 to 35 milliseconds. There are also other works that have ring-down time values that are comparable to the ones in this work [9]; however, they include delayed feedback loops in their RC systems.

There are numerous advantages coming with the proposed single-resonator RC setup, particularly in terms of practicality. The first is operation at ambient pressure, which eliminates the requirement for complex vacuum systems and makes the method more accessible to implement in real-world applications. This advantage also creates a faster system response due to the decrease in ring-down time of the resonator with a reduced quality factor as a result of atmospheric conditions. Nevertheless, it is possible to obtain a nonlinear response with the NEMS resonator despite the low quality factor (~ 50). The mentioned benefits, along with the low power consumption, have the potential to facilitate the introduction of edge-computation technologies and other applications in daily-life.

The simplicity of operation is not the only benefit that this system offers; it also takes advantage of the dynamics of NEMS. Considering that the decay time of NEMS resonators is on the microsecond scale, the experiments can be carried out in a matter of minutes. Additionally, the NEMS devices are compatible with assembly in a wide variety of applications due to their compact sizes. Therefore, all these novel properties of NEMS RC result in a more demonstrable system than the current state-of-the-art.

1.3 Thesis Outline

Chapter 1 begins with an introduction to the field of reservoir computing. Then, the motivation behind this thesis, namely reservoir computing with single non-linear NEMS resonators, is discussed in terms of the ability to combine the two mentioned technologies.

Chapter 2 begins by providing information on the design of NEMS devices. Next, the fabrication of NEMS devices is explained. Finally, the simulations performed to see the mode shapes expected from the fabricated devices are elaborated.

Chapter 3 begins with explaining the operating techniques used for NEMS devices. The characterization of the NEMS devices and the electronic circuit used in the experiments are presented. Later, the proposed setup of a reservoir computing structure with a nonlinear nanomechanical resonator is discussed. Finally, the theory behind the nonlinear model of NEMS devices is discussed.

Chapter 4 presents the MNIST handwritten digit recognition task used to evaluate reservoir computing with a single nonlinear NEMS resonator. Afterward, the ridge regression used in the training and testing algorithms to accomplish this task is mentioned. Finally, the validation method of the reservoir outputs is explained.

This thesis is concluded in Chapter 5 by reviewing the relevant findings and outlining future remarks.

Chapter 2

Design, Fabrication, and Simulation of NEMS Devices

2.1 Device Design

Device design is one of the most critical phases when employing NEMS for RC. It is possible to change the device design to change the device decay time and the required nonlinearity by considering the theory behind the NEMS resonator decay time and its nonlinear modeling expressions, which are functions of the device dimensions. The device design and fabrication also have a significant impact on the mechanical mode shapes and frequency stability of the devices. The frequency stability can be enhanced by clean fabrication.

There are two primary components that are essential to the functioning of doubly-clamped beam devices. These components are the resonator beam and the electrodes responsible for resonating the beam. The resonator beams are primarily fabricated from silicon nitride films that are deposited on top of silicon substrates, whereas the electrodes are mostly composed of gold and are put on top of the beams for the purpose of driving and reading from the resonator beam [10]. Therefore, it is essential to design the regions accurately, composed of nitride or gold, to get the desired parts at the end of the fabrication process. This objective is achieved by assigning each material and each component to the relevant layers throughout the design phase.

Since over-etching during the suspension of the mechanical beam structure would create a decrease in the quality factor of the resonator, it is crucial to design the pool region (opening in the nitride layer in the device design) in accordance with the required etching time calculated for the beam release. Furthermore, it is essential to design the electrodes to have impedance matching with the rest of the circuit in which the device will be used.

Pre-existing designs that were widely utilized within the Hanay group were used to fabricate the doubly-clamped beam devices employed in this study. The dimensions of the devices are often 10 μm in length, 0.4 or 0.8 μm in width, and 100 nm in thickness. It was decided that a device with a width of 0.4 μm would be the most suitable option for the purpose of adjusting the decay time in this work. In Section 2.2, the fabrication process of the devices is explained in detail. See the theses in the references [11–13] for more thorough discussions on fabrication. Figure 2.1 shows a widely utilized mask design for a doubly-clamped beam.

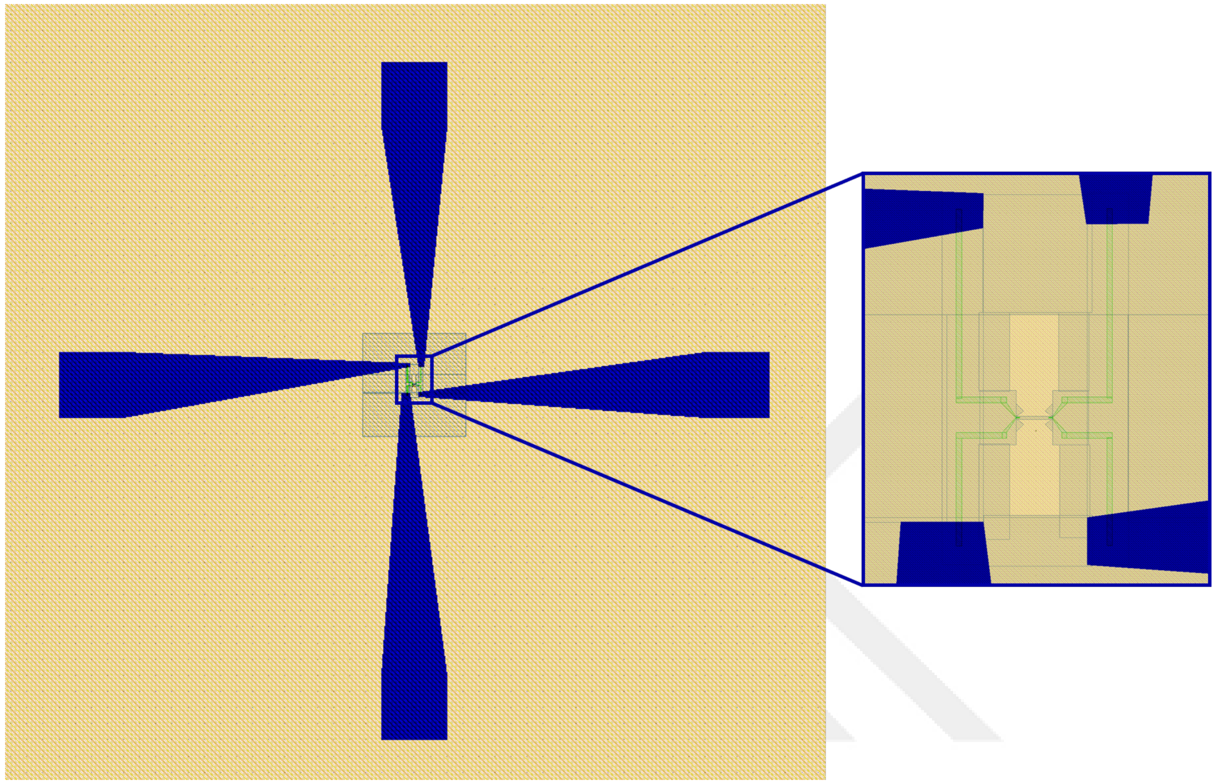

Figure 2.1: A conventional mask design for a doubly-clamped NEMS resonator.

In Figure 2.1, the yellow region corresponds to the silicon layer, the light blue region corresponds to the silicon nitride layer, and the dark blue and light green regions correspond to the gold layer. The gold parts are patterned in two layers in EBL for resolution adjustment. The design shown has dimensions of $4mm\,x\,4mm$, and a custom wafer measuring $34mm\,x\,34mm$ can accommodate $7x7$ of these designs.

2.2 Device Fabrication

The fabrication process elaborated in this thesis is also explained in detail in references [11–15]. The wafers used in the fabrication of the devices are acquired from the company University Wafer (Part No: 1917). These wafers have 100 nm LPCVD stochiometric silicon nitride films on both sides, with below 200 MPa film stress, on top of a doped 500 μm silicon substrate. The wafers are also one-side polished, and the fabrication is made on the polished side.

After preparing the wafer for fabrication, the process begins with electron beam lithography (EBL) for patterning gold electrodes [10,16,17]. **Steps II-VII** of the fabrication given below take place at Sabanci University Nanotechnology Research and Application Center (SUNUM).

Step I: A $4-inch$ wafer is coated with **AZ4533** photoresist, baked at 110° C for 60 s on the hot plate to improve the photoresist adhesion, and diced in $34mm\,x\,34mm$ parts. Photoresist coating is used to protect the wafer during the dicing process, and it is removed using acetone after dicing. The wafer is then washed in IPA and dried using nitrogen gas.

The following steps can be conducted for each of the $34mm\,x\,34mm$ parts. Also, for the sake of visualization, the illustrations in Appendix A are for a single device in the $7x7$ batch on one wafer part, as depicted on the inset of Figure 2.1.

Step II: To pattern the gold regions, the wafer is coated with bilayer Poly(methyl methacrylate) (**PMMA**) before the first EBL step. The wafer after coating PMMA can be seen in Figure A.1(a).

Step III: After coating PMMA, the gold regions are patterned with EBL, and the exposed PMMA is developed in a $MIBK : IPA$ solution (the mixing ratio is unknown since this step is conducted in SUNUM). Figure A.1(b) shows the wafer after development.

Step IV: To define the gold regions, the wafer is coated with 70 nm gold on top of a 5 nm chromium for adhesion. Figure A.2(a) shows the wafer after gold coating.

Step V: For the lift-off of the gold on the remaining PMMA after development, the wafer is washed in acetone and IPA and dried using nitrogen gas. Figure A.2(b) shows the wafer after lift-off.

Step VI: To pattern the copper etch mask for the silicon nitride region, which defines the resonator beam, the wafer is again coated with bilayer PMMA before the second EBL step. Figure A.3(a) shows the wafer after the second PMMA coating.

Step VII: The copper region is patterned with another EBL step, and the exposed PMMA is developed. Figure A.3(b) shows the wafer after the second development.

After receiving the wafer patterned with EBL from SUNUM, the rest of the steps are conducted at the Bilkent University National Nanotechnology Research Center (UNAM).

Step VIII: To define the copper etch mask region, the wafer is coated with 40 nm thermally evaporated copper. Figure A.4(a) shows the wafer after copper coating.

Step IX: For the lift-off of the copper on the remaining PMMA after development, the wafer is again washed in acetone and IPA and dried using nitrogen gas. Figure A.4(b) shows the wafer after the second lift-off.

Step X: Then the copper-coated wafer is again coated with **AZ4533** photoresist, baked at 110° C for 60 s on the hot plate, and diced in chips. 49 chips are obtained in the case of $7x7$ device mask design. The photoresist is not removed right after the dicing process to be used as protection for the back-etching of the silicon nitride, which is the non-polished side.

Step XI: The etching steps are done using Inductively Coupled Plasma (ICP). The ICP chamber is first cleaned with oxygen plasma and then preconditioned with silicon nitride etchant when empty. Then, the silicon nitride on the non-polished sides of the chips is etched, and the photoresist on the chips is removed using acetone. The chips are then washed in IPA and dried using nitrogen gas.

Step XII: The suspension of the resonator beam is done in two steps: Anisotropic silicon nitride etch to define the beam and then isotropic silicon etch to release the beam. The etchant recipes for silicon and silicon nitride are given in Table 2.1. The device suspended in ICP can be seen in Figure A.5(a).

Parameters	Silicon (Si)	Silicon Nitride (Si_3N_4)
Etchant Gas	CF_4	SF_6
Etchant Gas Flow Rate (sccm)	20	15
Passivation Gas	CHF_3	CHF_3
Passivation Gas Flow Rate (sccm)	3	2
Coil Power (Watt)	400	150
Platen Power (Watt)	100	30
Chamber Pressure (mTorr)	5	10
Etching Duration (s)	60	225

Table 2.1: ICP Etchant Recipes

Step XIII: After the resonator beam is released using ICP, the copper etch mask is removed using MicroChemicals TechniEtch **Al80** wet etchant. Figure A.5(b) shows the chip after copper etch mask removal and the device fabrication is completed.

In order to be able to use the fabricated chips in the experiments, they are placed on a custom-made printed circuit board (PCB) with SMA connectors. The gold bonding pads on the chips are connected to the SMA connector via aluminum wedge wire-bonds. The wire-bonding step takes place in the METU MEMS Center.

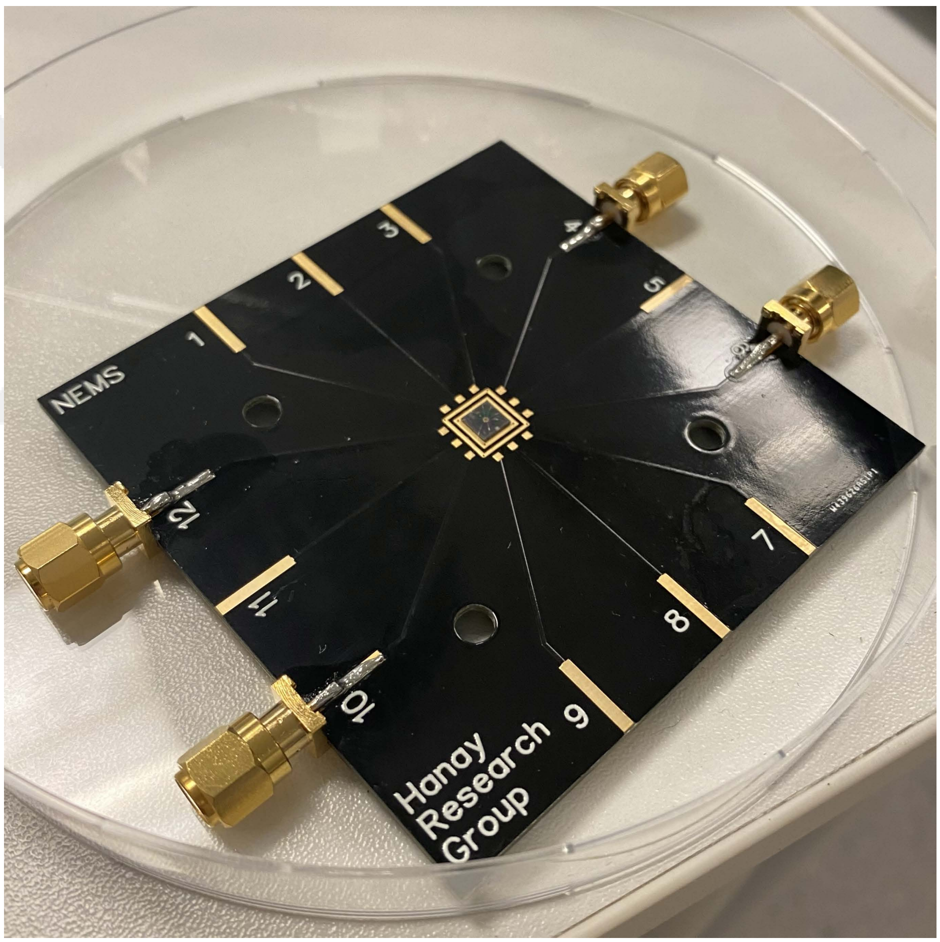

Figure 2.2: The wire-bonded chip on top of the PCB.

The wire-bonded chip on top of the PCB can be seen in Figure 2.2, and the SEM image of the fabricated device can be seen in Figure 2.3.

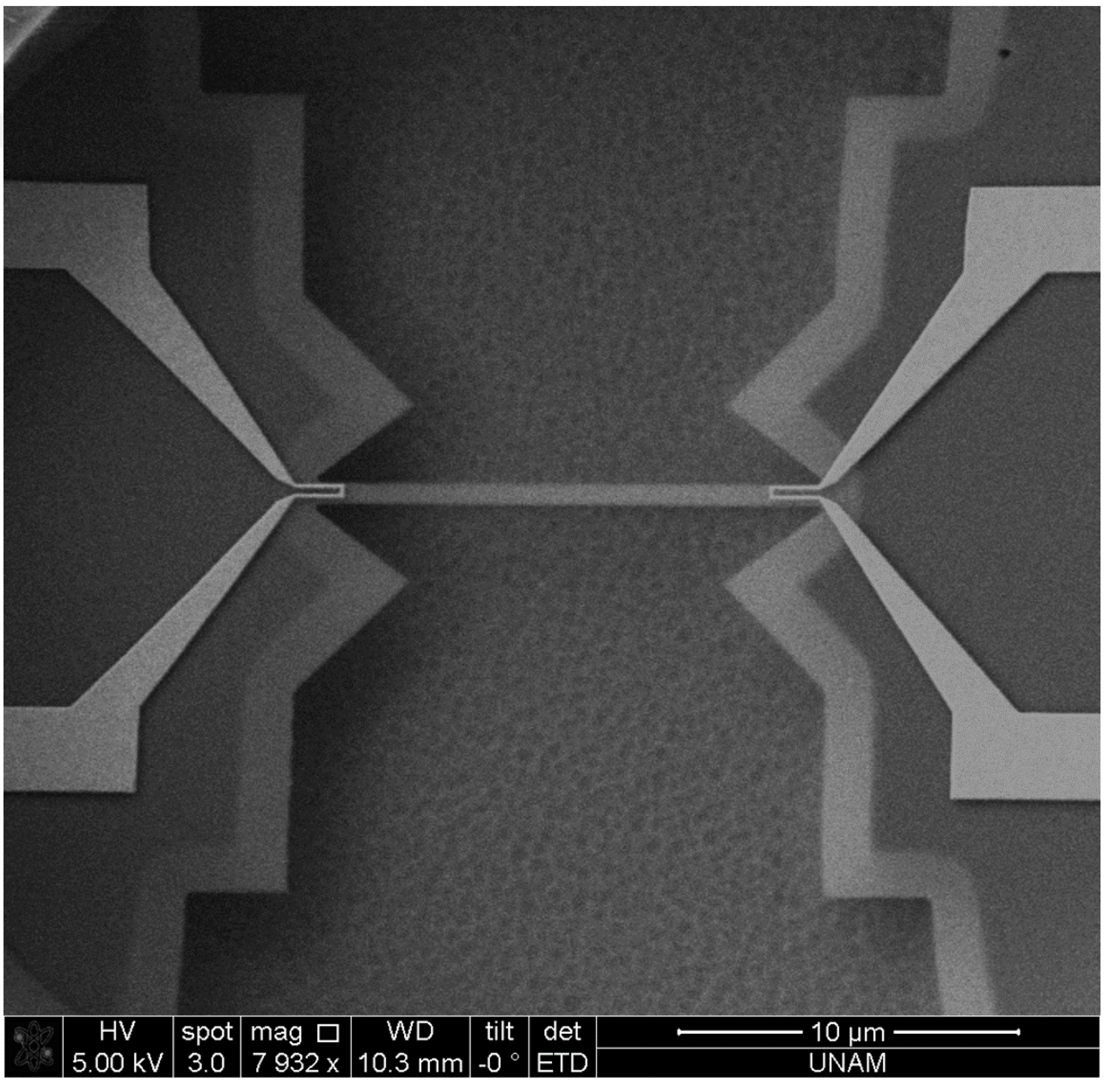

Figure 2.3: The SEM image of the resonator used in the experiments.

2.3 FEA Simulations

After the fabrication of the device is completed, finite element analysis (FEA) simulations are conducted to see the mechanical mode shapes of the resonator beam. This step is essential to interpret the resonance peaks appearing in the open-sweep frequency measurements of the device and to differentiate between the in-plane and out-of-plane modes since the experiments are done using out-of-plane ones.

In order to do this, the dimensions of the device after fabrication are measured using the ImageJ software on the SEM images of the device. The fabricated dimensions are used instead of the mask dimensions to enhance the precision of the simulations. After the dimensions are obtained, the mechanical mode shapes are calculated. During the calculation, the stress of the silicon nitride beam is adjusted in iterations so that the fundamental mode frequency matches the value obtained from open-sweep measurements. Since the nitride stress is claimed to be less than 200 MPa by the wafer vendor, the iterations start from 200 MPa and decrease. Eventually, the calculation was completed with 150 MPa nitride stress.

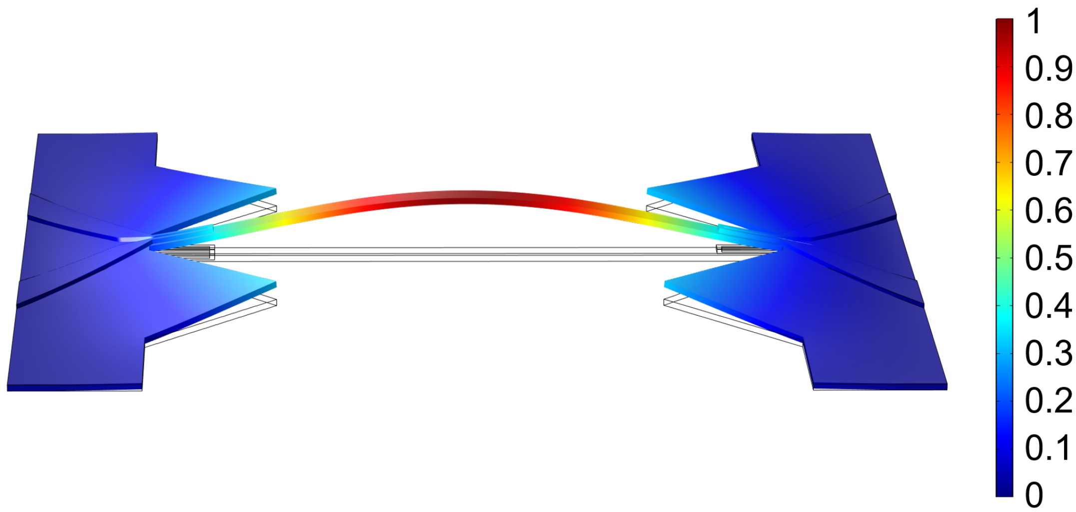

Figure 2.4: The fundamental mode shape of the device.

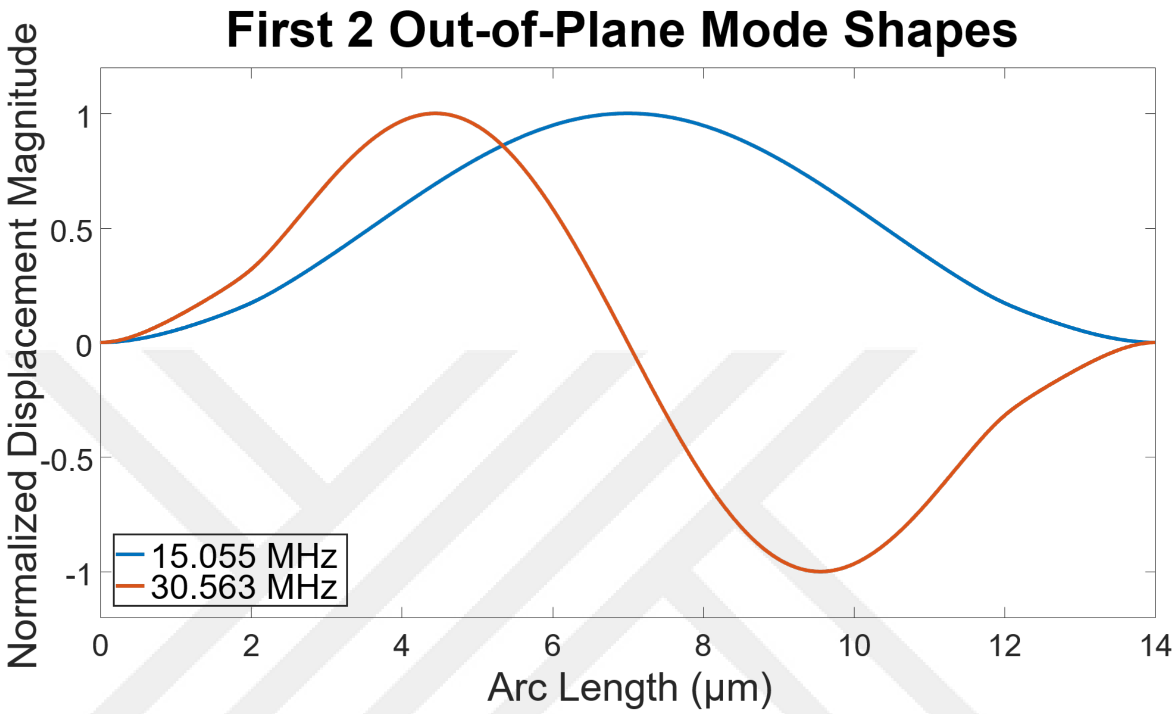

Figure 2.5: The first two mechanical mode shapes of the device simulated.

Figure 2.4 shows the fundamental mode of the device. Figure 2.5 shows the first two out-of-plane mechanical mode shapes of the fabricated doubly-clamped NEMS for this study.

The frequency values shown in Figure 2.5 will be compared to the open-sweep frequency measurement values in Section 3.2.

Chapter 3

Experimentation and Theory

3.1 Driving and Reading Scheme of NEMS

The doubly-clamped NEMS devices presented in this thesis operate with thermoelastic actuation and piezoresistive detection [10, 18].

Thermoelastic actuation works by putting two materials with different thermal expansion coefficients on top of each other. With the devices used in this thesis, the two different materials are the silicon nitride (resonator beam) and the gold (electrodes). Since the thermal expansion coefficients of nitride and gold are different, applying AC voltage to the gold electrodes leads to varying degrees of thermal expansion on both the electrodes and the beam, resulting in differing elongations. This situation induces stress propagation along the beam, resulting in resonance. The heating of the gold electrodes is directly proportional to the square of the amplitude of the applied AC voltage. As a result, the frequency of the beam oscillation (ω) is twice the frequency of the applied AC voltage ($\omega/2$) [19]. This outcome is also shown in the following section in Figure 3.2.

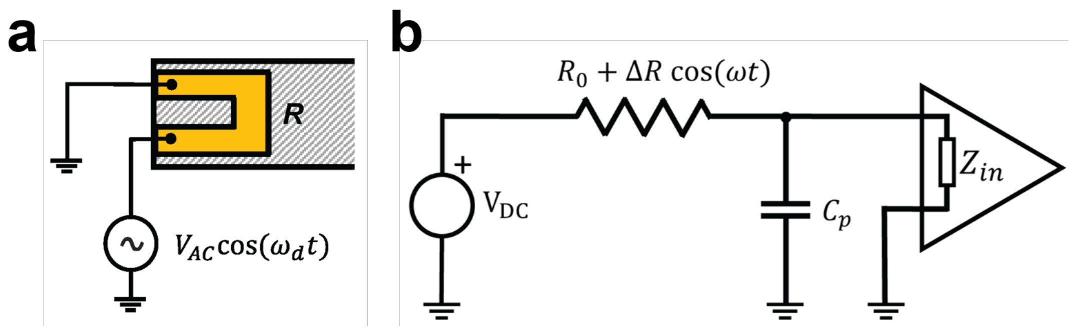

Figure 3.1: The thermoelastic actuation **(a)** and piezoresistive detection **(b)** diagrams, adapted from [19]

Piezoresistive detection works by detecting the resistance change that occurs on the gold electrode (that is not used for actuation) due to the oscillation of the doubly-clamped beam. A bias-tee is included in the setup to facilitate the detection of resistance variations while the NEMS can be driven. For this, the DC port of the bias tee was supplied with a constant voltage with a slightly higher value than the NEMS driving voltage. Since the displacement magnitude of the beam is maximum at resonance, the resistance change value is also maximum at resonance, and these values are seen in the open-sweep as peaks in amplitude. Notably, the electrodes of the NEMS devices are specifically built to have a resistance of $50\,\Omega$ in order to match the impedances with the Lock-in-Amplifier, which has an input impedance of $50\,\Omega$. Figure 3.2 displays the NEMS electrodes and the other components of the circuit.

3.2 Device Characterization

Before starting each experiment, the NEMS devices are characterized by checking their open-sweep frequency measurements to determine their resonance frequencies. The circuitry for open-sweep measurements includes a Lock-in-Amplifier (Zurich Instruments HF2LI), a bias tee, and a low-noise amplifier. Figure 3.2 shows the open-sweep measurement circuit used for NEMS devices.

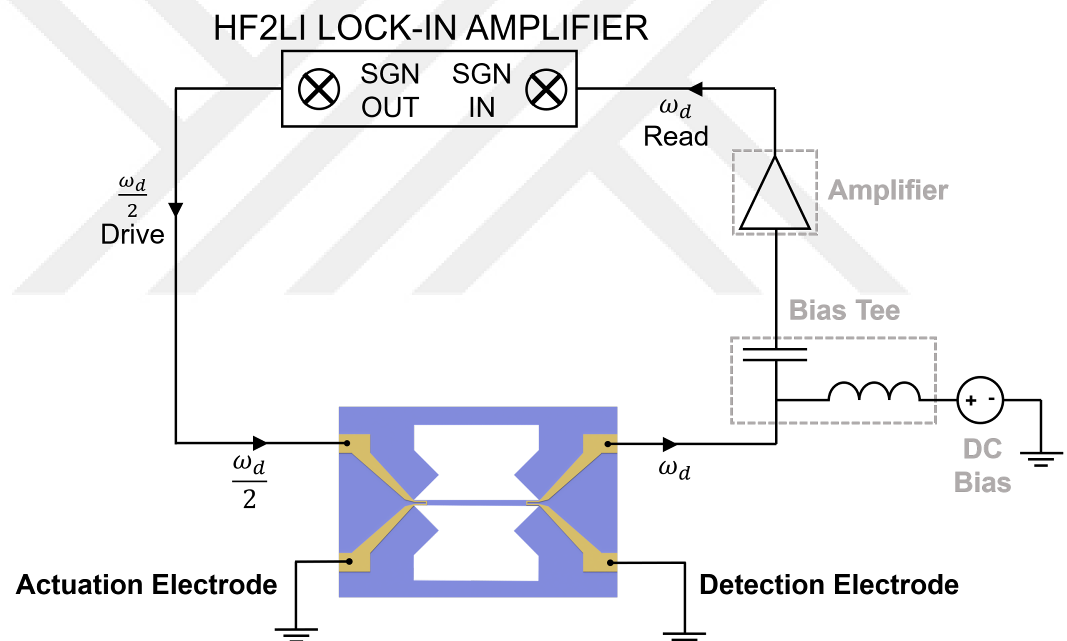

Figure 3.2: The circuit used in open-sweep measurements of the NEMS devices.

The driving signal is provided by the signal output of the lock-in-amplifier (LIA), and the readout signal is collected by its signal input. Since the reading is performed by piezoresistive detection, the readout signal goes through a bias-tee supplied with a constant voltage from its DC port to create a voltage drop to facilitate the resistance change measurement. Then, this signal goes through an amplifier to enhance the correlation between elongation and voltage drop collected by the LIA for improved reading.

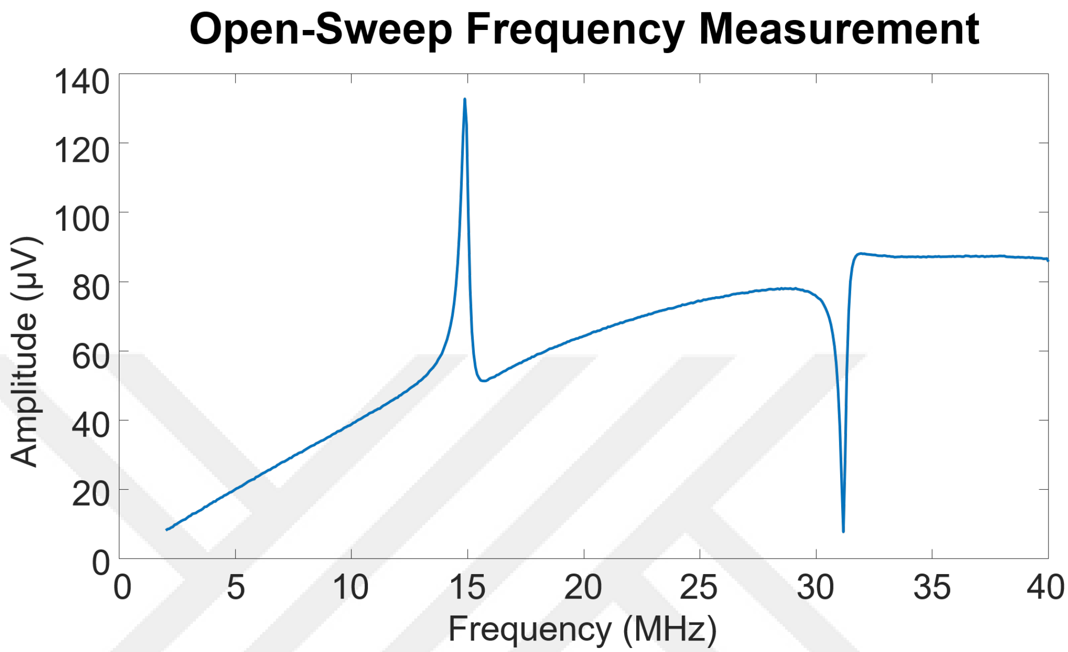

Figure 3.3: The open-sweep frequency measurement of the regular doubly-clamped NEMS device used in the experiments from 2 MHz to 40 MHz.

The open-sweep frequency measurement of the device before the experiment is shown in Figure 3.3. In the open-sweep data, the first two modes also appear at $\sim 15\ MHz$ and $\sim 30\ MHz$, as was shown in mode shape simulations in Figure 2.5. Since the experiments are conducted using the fundamental mode, higher mechanical modes were not necessary to be measured.

3.3 Experimental Setup

The experiment setup used for the single nonlinear NEMS resonator RC consists of a custom NEMS resonator, an Arbitrary Waveform Generator (Keysight 33600A Series), a Lock-In Amplifier (Zurich Instruments HF2LI), and a laboratory workstation. Moreover, a DC power supply, an amplifier, and a bias-tee are used to complete the drive and readout circuit of the NEMS device. In order to identify the parameters for each experiment, an open-loop frequency sweep is performed using the LIA to determine the optimal driving frequency and the quality factor for the designed RC system.

For the purpose of modulating the driving signal with the input data and then feeding the modulated signal to the NEMS for the RC system, an arbitrary waveform generator (AWG) is utilized in the experimental setup, as depicted in Figure 3.4. A vectorized representation of the pixel color information of the images is included in the input data. On the other hand, the driving signal is configured to be a sinusoidal wave with the frequency and amplitude of the chosen nonlinear state of the resonator. The amplitude modulation (AM) takes place in accordance with Equation 3.1.

$$V_{drive} = m(t)V_d cos(\omega_d t) \tag{3.1}$$

where V_d is the nonlinear driving amplitude given to the AM, $m(t)$ represents the brightness of each pixel normalized to between 0 and 1, and ω_d is the nonlinear driving frequency of the resonator ($2\pi f_d$). The AM frequency is the factor that determines the value of t in $m(t)$ when the sample number is divided by the AM frequency.

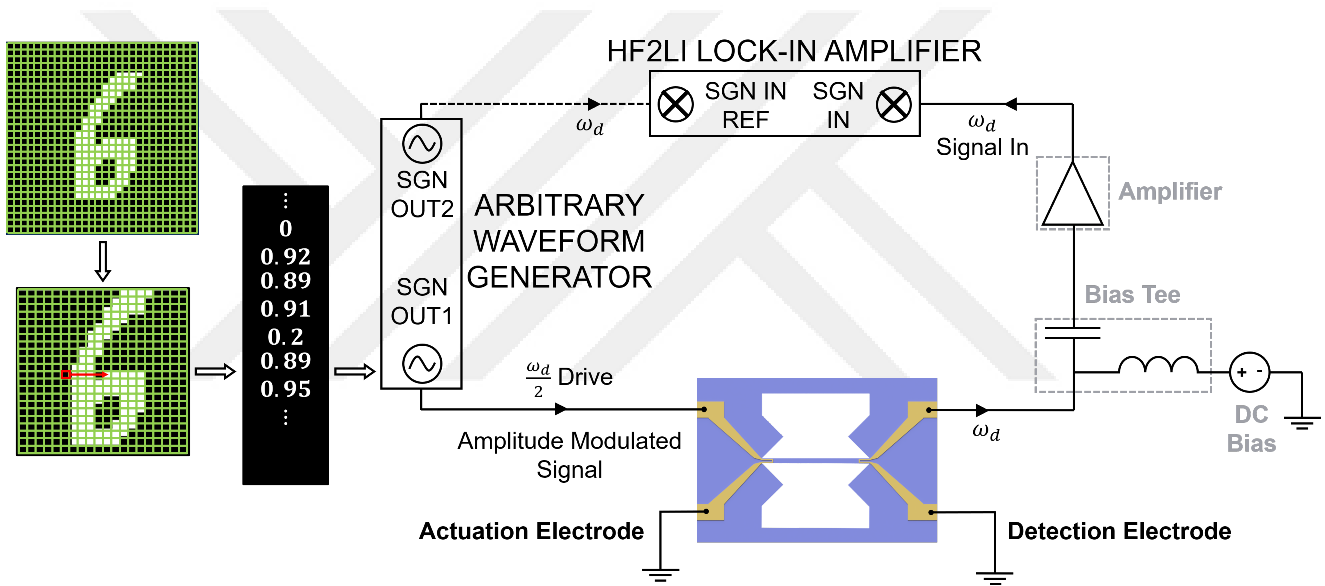

Figure 3.4: Schematic of the experimental setup and reservoir computing system. Cropped images with high information content are uploaded to the arbitrary waveform generator as vectors with grayscale values corresponding to the pixel brightness (normalized to unity). The rendered CAD drawing of the resonator is in the bottom middle of the circuit schematic. The actuation electrode of the resonator receives an AC signal (sinusoidal wave) that has been modulated with the input vectors. The LIA is used to read through the detection electrodes using an external reference signal from AWG.

The output signal coming from the NEMS resonator driven by the forenamed modulated signal is read by an LIA. The readout takes place through the process of demodulating the output signal of the NEMS using a reference signal provided by the second channel of the AWG. This reference to the LIA is also a sinusoidal wave, which is the second harmonic of the signal used in amplitude modulation with 1V amplitude for demodulation optimization purposes. The signal is the second harmonic of the driving signal because the thermoelastic actuation of the resonator creates mechanical strain at double the driving frequency, resulting in a readout frequency that is twice the input frequency. Therefore, the LIA is configured to demodulate the output signal at twice the resonator driving frequency, leveraging this reference signal. After the readout of the nonlinear reservoir is collected, it is used for the training and validation step.

This RC setup offers a multitude of advantages owing to its single-resonator structure. Firstly, it is less complicated than the majority of other RC applications yet is practicable and efficient in information processing. The integration of AWG into the setup to modulate the input data with the resonator driving signal eliminates a significant number of software and hardware implementations in most of the other works. Moreover, using LIA to demodulate the output signal results in a smooth readout process.

3.4 Nonlinear Model of the NEMS Reservoir

A doubly-clamped silicon nitride beam with dimensions of 10 μm length, 0.4 μm width, and 100 nm height is used as the resonator, which is the main part of the nonlinear RC system. The performance of the RC system is significantly affected by the natural frequency and the quality factor (Q) of the NEMS. A high Q is needed to obtain a sufficient memory capacity since it involves the ring-down time ($T = \frac{2Q}{\omega_n}$) of the resonator. Multiple frequency sweeps are performed for the characterization of the nonlinear dynamic response of the NEMS and to determine the optimal driving frequencies (f_d) and amplitudes. This step is crucial to obtain the desired nonlinear state, which determines the richness of the reservoir.

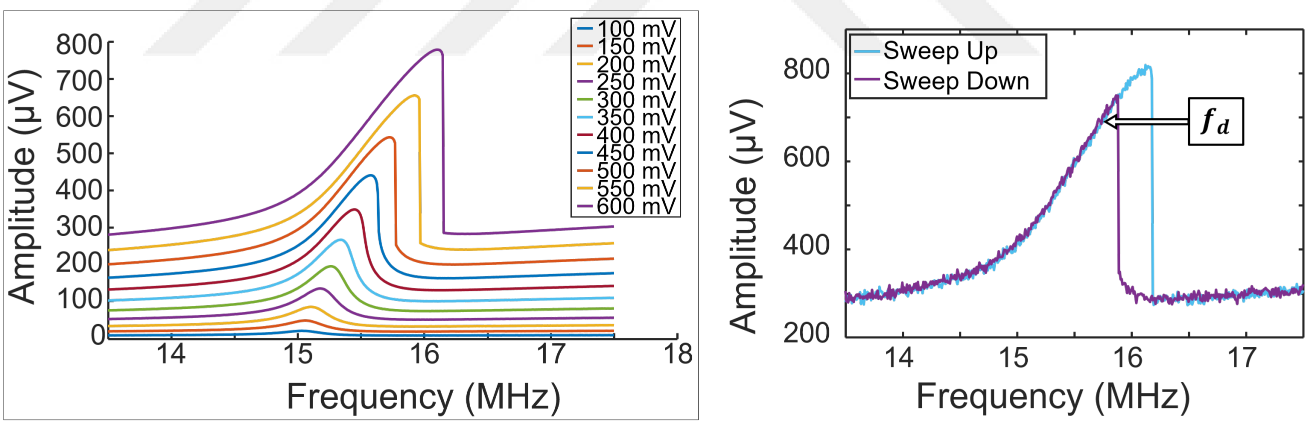

Figure 3.5: Linear to nonlinear frequency open-sweeps with regular doubly-clamped NEMS resonator. **(a)** Multiple frequency open-sweeps are taken to discover the nonlinear response of the NEMS resonator. **(b)** Open-loop frequency sweep of the nanoelectromechanical resonator at its first mode under atmospheric conditions. The frequency indicated by the black arrow is the nonlinear driving frequency of the resonator, 15.8 MHz, whereas the linear natural frequency of the resonator is 15.05 MHz.

The nonlinear frequency response of the first mode of the NEMS resonator that was used in the experiments can be observed in Figure 3.5. As demonstrated in the figure, the resonator was driven at a frequency (f_d), which is slightly lower than the front bifurcation point frequency to prevent the switching between two stable points since the resonance peaks of the resonator drift backward in frequency due to the heating of the resonator over time [20]. However, the chosen frequency is not much lower than the front bifurcation point to ensure a high signal-to-noise ratio. So, an optimal point for f_d should be determined to meet these requirements.

3.4.1 Theory of the Nonlinear Model

The NEMS resonator used in the experiments behaves as a typical second-order underdamped oscillator. The combination of the Duffing nonlinearity arising from the restoring force of the resonator and the exponential transient nonlinear response associated with its second-order dynamics creates a nonlinearity within the system. This combination results in efficient processing of the MNIST handwritten digit recognition task implemented in the system owing to the richness of the nonlinearity within the single resonator reservoir.

The resonator is driven by thermoelastic actuation, and its readout is collected as piezoresistive. The Duffing nonlinear equation shown in Equation 3.2 approximates the displacement of the resonator, in the regular doubly-clamped NEMS case.

$$\ddot{x} + 2\zeta\omega_n\dot{x} + \omega_n^2 x + \alpha x^3 = F_d(t) \tag{3.2}$$

where $\ddot{x}$, $\dot{x}$, and x are the acceleration, velocity, and displacement of the resonator, respectively. ζ and ω_n are the damping ratio and the natural angular frequency of the resonator in the linear regime, respectively. $F(d)$ is the time-dependent driving force per unit mass. The Duffing term is included in the equation by the coefficient α, which controls the amount of nonlinearity.

Equation 3.3 provides an estimation of the value of α in the context of doubly clamped beams.

$$\alpha = \frac{32E}{\sqrt{2\rho L^4 A}} \tag{3.3}$$

where A is a constant term of $2x10^{-10}$, ρ is the density of the beam, L is the length of the beam, and E is the Young's modulus of the nitride. The α of the resonator used in this work is calculated as approximately $2.56x10^{21}\ \frac{Hz^2}{m^2}$ using Equation 3.3.

The analytical solution for the displacement of the resonator becomes Equation 3.4 when the beam oscillates linearly with $\alpha = 0$, i.e., no nonlinear term.

$$x(t) = 1 \pm \frac{e^{-\frac{\omega n}{2Q}t}}{\sqrt{1-(\frac{1}{2Q})^2}} \tag{3.4}$$

The exponential term is named transient nonlinearity when the initial condition is $F_d(t) = 0$. In order to enhance the richness of the nonlinear dynamics of the system, the relation between the transient term and the Duffing term is essential.

The MNIST handwritten digit dataset is utilized in order to evaluate the classification performance of the system after the specified beam parameters have been determined. It is demonstrated that the proposed single nonlinear NEMS resonator RC model has an efficient information processing capacity, as evidenced by an average classification accuracy of 81.5% achieved.

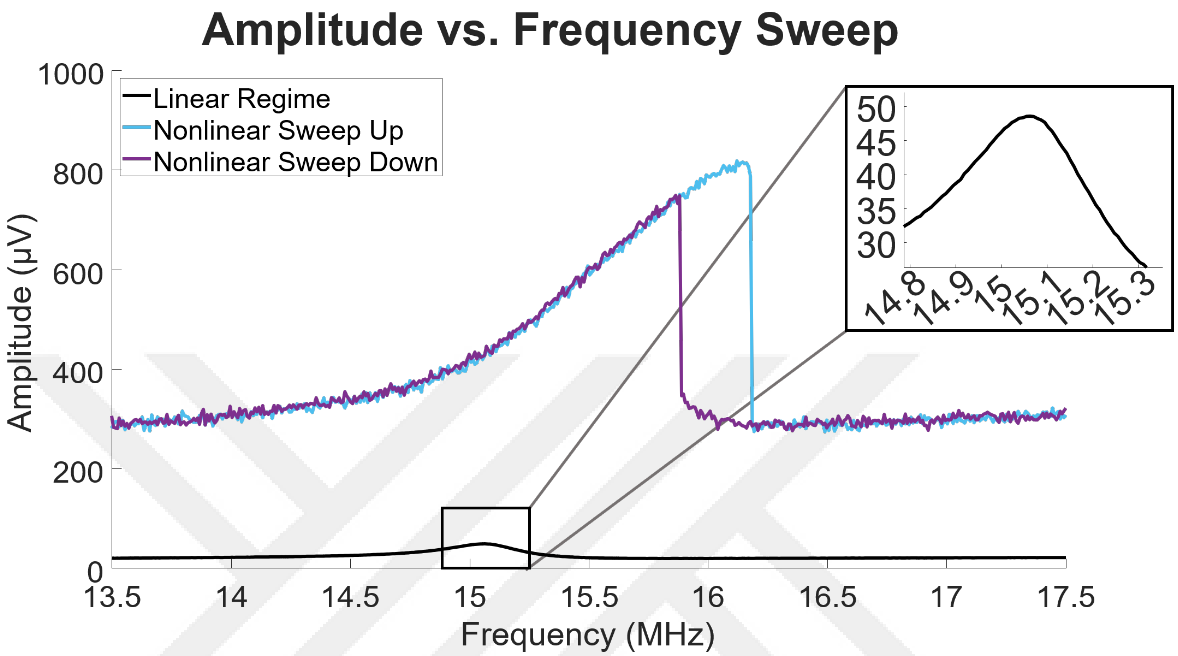

Figure 3.6: The linear and nonlinear frequency sweeps of the regular doubly-clamped NEMS resonator.

Figure 3.6 illustrates the comparison between the linear and nonlinear regimes. A linear response is obtained when the applied drive amplitude is $V_{AC} = 250\,mV$, the black curve in Figure 3.6, which can be observed more clearly on the inset. A nonlinear response is obtained when the applied drive amplitude is $V_{AC} = 490\,mV$, the purple and cyan curves, sequential and reverse sweeps, respectively. Considering the lack of symmetry in both the sequential and reverse sweeps, unlike the linear curve, it is evident that the response is nonlinear and exhibits spring-hardening characteristics with a gradual increase in amplitude but an abrupt decrease at a frequency higher than the linear driving frequency.

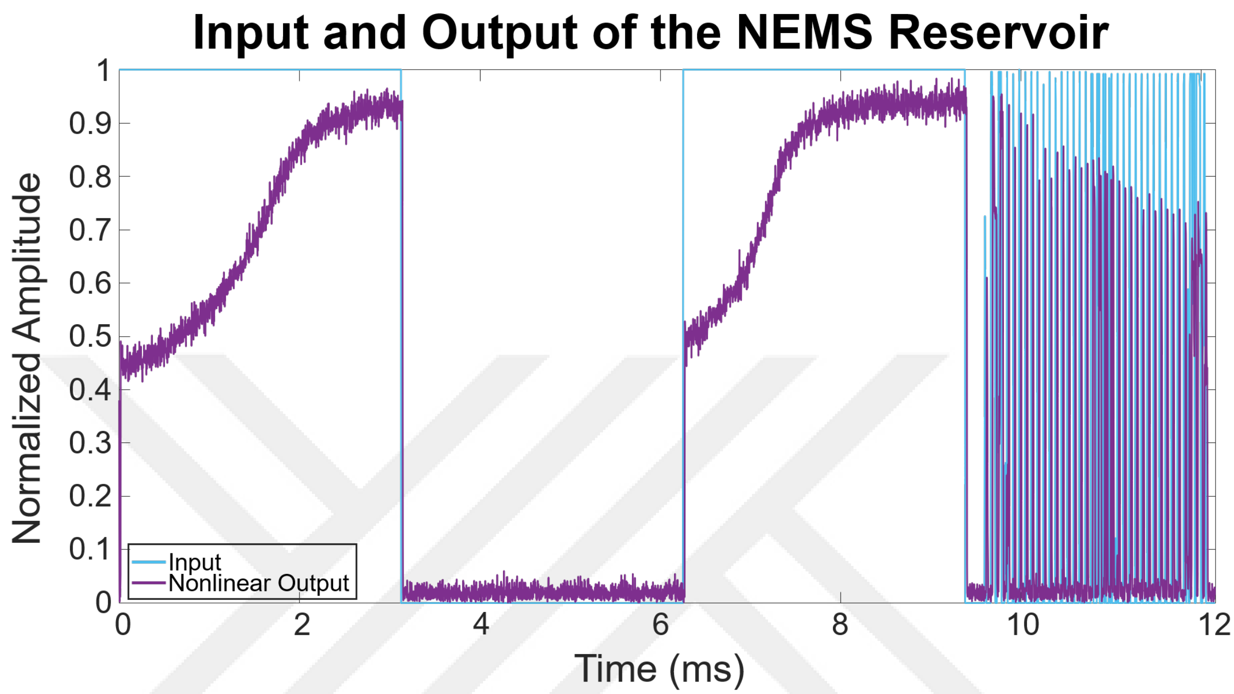

Figure 3.7: The input and the output signal of the regular doubly-clamped NEMS reservoir. The effect of the nonlinearity is seen in the difference in amplitude level. The nonlinear output is also transient.

As demonstrated in Figure 3.7, a fading memory effect occurs at the readout of the resonator as a result of its transient nonlinear dynamics. This transient dynamics, originating from the use of separation times below the decay time of the resonator, causes each data point to be influenced by the previous data points, ultimately resulting in a memory behavior.

Chapter 4

Experiment Results and Analysis

4.1 MNIST Handwritten Digit Recognition Task

The nonlinear information processing performance of the nonlinear NEMS resonator and the classification performance of the single-NEMS RC are evaluated by the MNIST handwritten digit dataset recognition task. The MNIST dataset, consisting of 28x28 pixel images, is a widely recognized benchmark for classification tasks in the field of handwritten digit classification. It is also well-defined for the purpose of testing the nonlinear mapping capacity of the NEMS reservoir, as illustrated in Figure 3.4. A set of 1000 images were randomly chosen from this dataset and given to the resonator as the input data modulated with the driving signal. While randomly chosen 900 images were used in the training algorithm, the remaining 100 were used to test the algorithm and calculate the classification accuracy.

The preprocessing of the selected MNIST images starts with cropping the images in 22x20 pixels to remove the redundant black periphery and make the input data to the reservoir (Figure 3.4) more informative. Afterward, the cropped images are vectorized and converted to vectors consisting of 440 elements to be compatible with the experiment setup since the input to the resonator should be a vector.

After creating the input as a vector consisting of 1000 subsequent 440-element vectors, the experiment parameters influencing the reservoir dynamics were set by trying different separation times. The separation time defines the time between two data points, i.e., two pixel values, as $\theta = n.T$ ($n \epsilon Z^{+}$) where T represents the decay time of the NEMS resonator.

Eventually, the input to the reservoir consisting of 1000 randomly chosen MNIST images containing 440 pixel value elements was used to test the performance of the proposed RC system. The 440 pixel values, i.e., the 440 data points, represented 440 artificial neural nodes responsible for information processing of the input signal within the NEMS reservoir.

After the acquisition of the readout data, the postprocessing step starts by converting the 1000-image output vector into a 1000x440 matrix. The training process is implemented using ten different linear classifiers with a "winner-takes-all" scheme. In this method, each handwritten digit class, ranging from 0 to 9, has its own classifier. Each classifier operates as a binary classifier, producing a value of ***1*** if the data being processed corresponds to the target class and a value of ***0*** if it does not. Then, the postprocessed data is split into a training set of 900 images and a testing set of 100 images randomly. The accuracy values are calculated using k-fold validation with 600 randomized folds, details explained in Section 4.4.2. An average classification accuracy of about 81.5% is achieved as a result of this task.

These results showcase the efficient information processing performed by the nonlinear NEMS reservoir and the effectiveness of the RC architecture proposed. The performance can further be optimized by modifying the nonlinear dynamics for various classification tasks.

The accuracies obtained by using the MNIST handwritten digit recognition task to test the proposed RC system show that its short-term memory has the potential to be used for simple forecasting tasks, and its efficient information processing makes it suitable for pattern recognition tasks. The single-resonator RC system, which works under ambient pressure and at higher speed, offers a more feasible and simplified system.

4.1.1 Effect of the Separation Time

In RC with NEMS, the choice of separation time is essential since it determines the frequency at which the input signal is updated. This separation timescale defines the duration of each sample point, i.e., the pixel value provided to the NEMS resonator. Therefore, if it is chosen close to or larger than the ring-down time ($\frac{2Q}{\omega_n}$) of the resonator, the resonator dynamics start switching from transient to steady state, resulting in a reduction in its memory capacity. On the other hand, choosing the separation time too small ($< 0.1\ t_{ring-down}$) has a detrimental impact on the mapping ability of the reservoir, which is required for the upcoming classification tasks.

The choice of the separation time acts as a determining factor in the feeding rate of the input data into the NEMS reservoir. The output is transient when the separation time is lower than the ring-down time of the resonator, and the output becomes steady as the separation time goes above the ring-down time. In RC studies, it is preferable to have small separation times since the transient dynamics enhance the fading memory effect of the reservoir.

4.2 Experiments with a Regular Doubly-Clamped NEMS

The first run of the experiments is conducted using a regular doubly-clamped NEMS resonator. The effect of different separation times was not observed for the parameters tried so far, as can be seen in Table 4.1. Since the ring-down time ($6.25\mu s$) of the resonator creates a lower time value of $\theta = 0.2T$ ($1.25\ \mu s$) to be provided and measured by the setup, even lower separation times were restricted by physical constrictions such as measurement speed. For further accuracy comparisons, a more advanced measurement system could be used to explore lower separation times. This outcome highlights the significance of the reservoir nonlinearity optimization to be applicable in more classification tasks.

Separation Time	Average Accuracy
$1.25\ \mu s$	80.5%
$1.88\ \mu s$	80.9 %
$3.125\ \mu s$	81%
$5\ \mu s$	81.5%

Table 4.1: Regular Doubly-Clamped NEMS Accuracy Statistics

A visual representation of the same digit input that is influenced by varying separation times and the results obtained from the single nonlinear NEMS resonator RC structure is depicted in Figure 4.1. This outcome shows that the NEMS reservoir is functional below $5\ \mu s$ operational speed and capable of achieving classification accuracies above 80%.

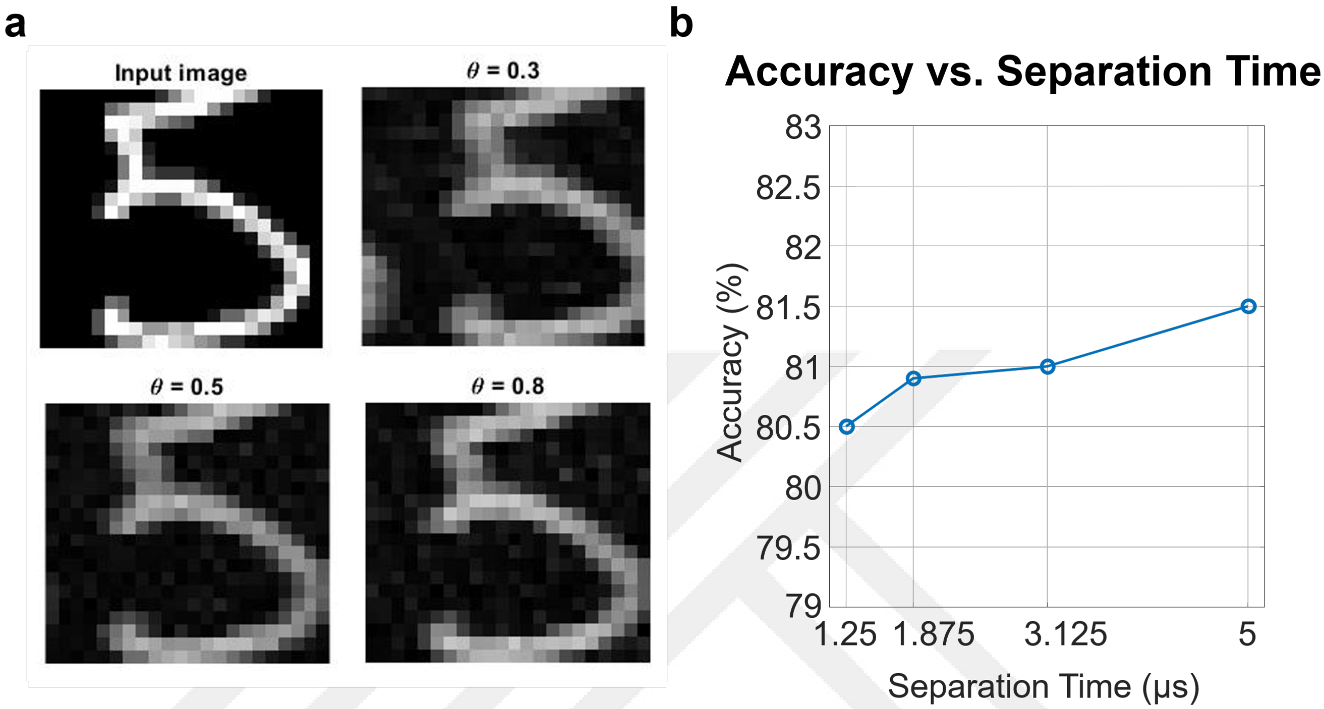

Figure 4.1: Effect of the separation time with regular doubly-clamped NEMS resonator. **(a)** The image of the same digit input at different separation times. **(b)** The comparison of the obtained average accuracy values based on the separation time. The test conditions are: $Q = 48.72,\ f_d = 15.6\,MHz,\ V_{DC} = 1\,V,\ V_{AC} = 490\,mV,\ T = 6.25\,\mu s$.

Following the performance evaluation with the MNIST handwritten digit dataset, the experiments conducted with a single nonlinear regular doubly-clamped NEMS resonator yielded a classification accuracy of 81.5%, demonstrating that NEMS technology has the potential to be used in physical RC systems. The confusion matrices of the predicted results with the average accuracies for no NEMS case and nonlinear regular doubly-clamped NEMS are shown in Figure 4.2.

It is evident that, while the total accuracies are the same for the confusion matrices displayed in Figure 4.2, there are variations in the correct predictions for some digit classes. The algorithm is challenged the most in recognizing the digits **5** and **8**; however, the inclusion of the nonlinear NEMS reservoir improved the classification performance of those digits. The classification performance for the remaining digits is approximately equal in both cases. Therefore, it can be hypothesized that the classification accuracy of the nonlinear NEMS case may exceed that of the no NEMS case once the nonlinear NEMS RC architecture is optimized for improved classification of the challenging digits.

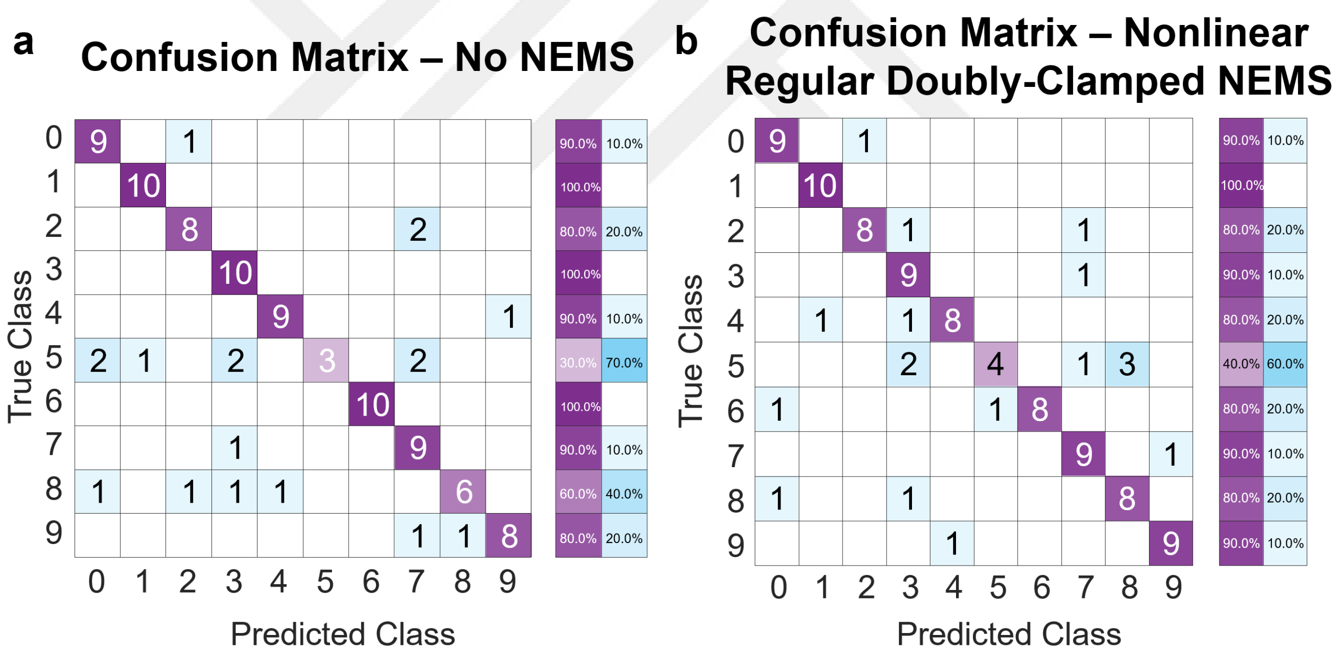

Figure 4.2: MNIST handwritten digit recognition using the reservoir computing system with regular doubly-clamped NEMS resonator. Confusion matrices of the predicted results with the average accuracies for no NEMS case **(a)** and nonlinear regular doubly-clamped NEMS **(b)**.

4.3 Experiments with a Paddle NEMS

The second run of the experiments is conducted using a paddle NEMS resonator [13, 21]. In order to overcome the limitation imposed by the ring-down time of the resonator in the previous experiments, a paddle NEMS device with heavier mass and, consequently, lower frequencies is utilized in this section. This approach aims to obtain a higher ring-down time value and explore a wider range of separation times. Nevertheless, the impact of varying separation times was not observed for the parameters tested so far, as seen in Table 4.2.

Separation Time	Linear Regime Average Accuracy	Nonlinear Regime Average Accuracy
1.8 μs	75%	74%
3.61 μs	75%	77%
7.21 μs	73%	73%
14.42 μs	72%	
28.84 μs	72.5%	77%
57.68 μs	76%	74%
115.36 μs	73%	75%

Table 4.2: Paddle NEMS Accuracy Statistics

The linear and nonlinear driving parameters are determined based on the plots shown in Figure 4.3 obtained during the experiments, along with the fundamental mode of the device utilized. Due to their increased weight compared to regular doubly-clamped NEMS devices, the paddle NEMS devices have a lower resonance frequency than those presented in the previous sections. Furthermore, the nonlinear regime is reached at a higher driving amplitude, with an onset of nonlinearity at 450 mV amplitude. The linear driving parameters consist of a frequency of 8.04 MHz and an amplitude of 400 mV, whereas the nonlinear driving parameters consist of a frequency of 8.07 MHz and an amplitude of 700 mV.

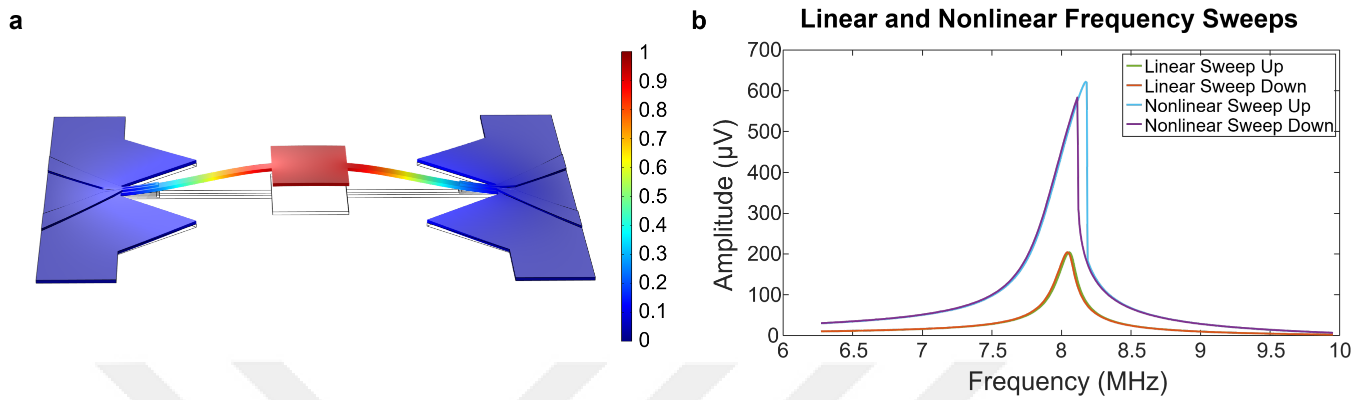

Figure 4.3: The paddle NEMS resonator and its linear and nonlinear frequency sweeps. **(a)** The fundamental mode shape of the device. **(b)** Linear to nonlinear frequency open-sweeps.

Figure 4.4 depicts the first two out-of-plane mechanical mode shapes and their corresponding frequency values from both the simulation and the open-sweep measurements, and it is evident that the values are in agreement.

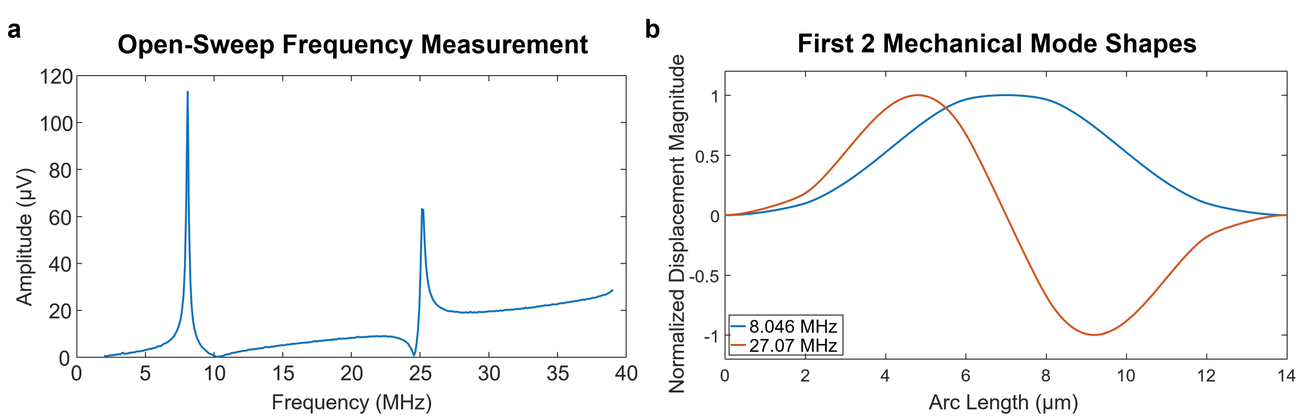

Figure 4.4: The mechanical mode frequency values from simulation and open-sweep measurements. **(a)** The open-sweep frequency measurement of the regular doubly-clamped NEMS device used in the experiments from 2 MHz to 40 MHz. **(b)** The first two mechanical mode shapes of the device simulated.

Following the performance evaluation with the MNIST handwritten digit dataset, the experiments conducted with a single nonlinear paddle NEMS resonator yielded an average classification accuracy of 75% in the nonlinear regime and 73.8% in the linear regime, demonstrating that the nonlinearity of NEMS is indeed generating data mapping ability. The confusion matrix of the predicted results with the average accuracy is shown in Figure 4.5.

The confusion matrices shown in Figure 4.5 clearly indicate that the classification performance of the paddle NEMS reservoir is insufficient to reach at or exceed the performance of the no NEMS case. Although the total accuracies of the confusion matrices for the linear and nonlinear paddle NEMS cases are comparable, it is apparent that the linear paddle NEMS had greater difficulty in data processing. The experiment results still demonstrate the challenge in recognizing the digits **5** and **8** for all cases. However, while the highest false positive rate is 5% in no NEMS case and 7% in nonlinear case; it is 19% in the linear case, which is for digit **8**. Thus, it can be deduced that the challenge is not solely caused by the algorithm but also by the data processing performed by the reservoir dynamics of the linear NEMS. A potential explanation for this result is that the digit class **8** has the highest amount of white pixels, and since white pixels have a larger pixel value multiplier, the NEMS nonlinearity has a stronger impact on the data for white pixels during the experiments. Hence, the digit **8** has a greater disparity in data processing across the linear and nonlinear regimes compared to the other digit classes. So, it can be inferred that the linear dynamics fails to achieve the linear separability of the data resulting from the nonlinearity. This situation results in the given high false positive rates, and it undermines the reliability of the accuracy result of the linear NEMS and the comparison between the accuracies of the linear and nonlinear NEMS.

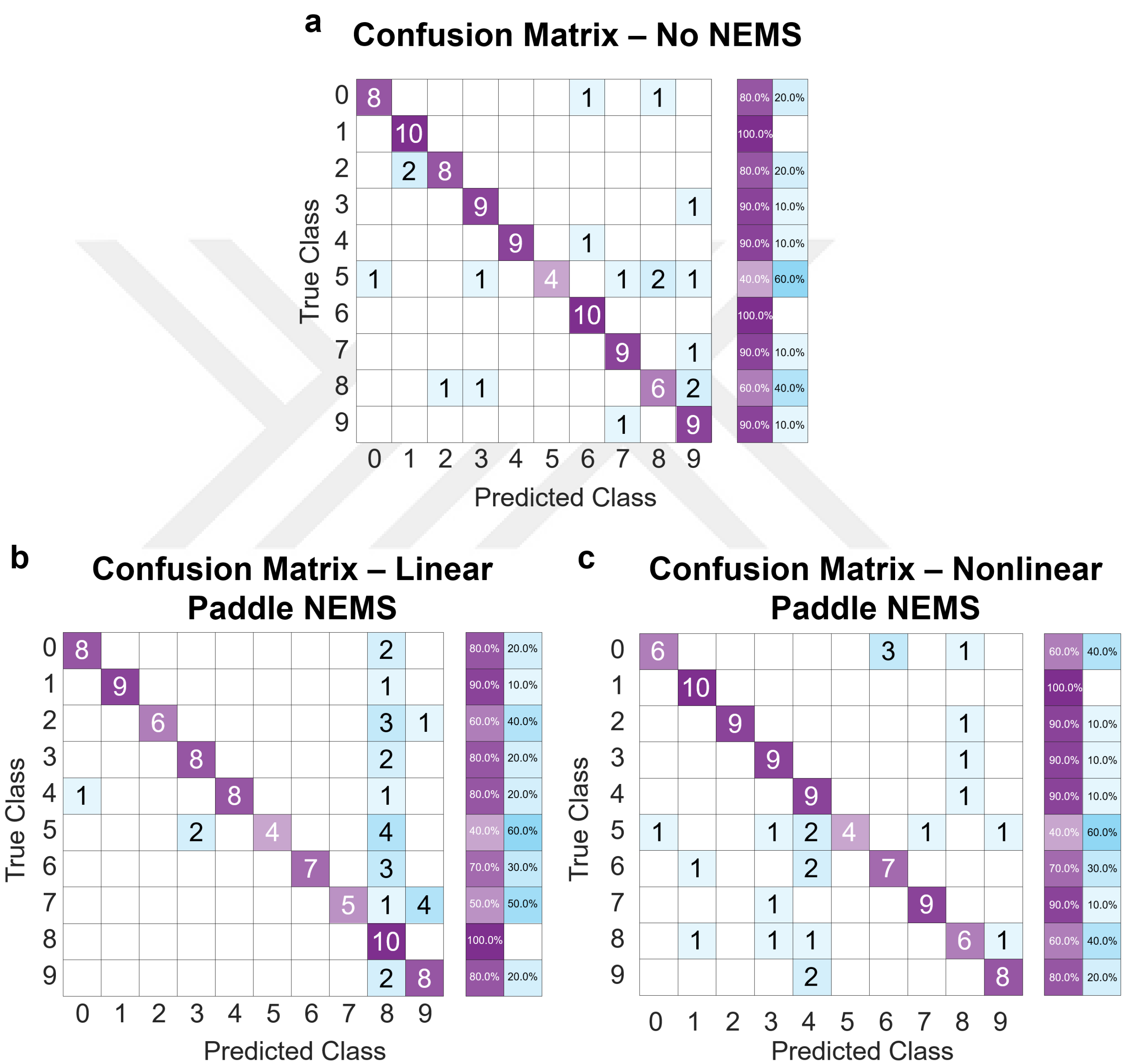

Figure 4.5: MNIST handwritten digit recognition using the reservoir computing system with paddle NEMS resonator. Confusion matrices of the predicted results with the average accuracies for no NEMS case **(a)**, linear paddle NEMS **(b)**, and nonlinear paddle NEMS **(c)**.

Figure 4.6 displays a graph illustrating the results obtained from the single nonlinear paddle NEMS resonator RC structure. The classification accuracies achieved by employing both the linear and nonlinear regimes of the paddle NEMS are compared to the case where training is performed without a NEMS. Contrary to predictions, the accuracy of the no NEMS case is the highest, while the average accuracies of the linear and nonlinear paddle NEMS examples are similar. This might be attributed to the presence of noise in the data processing with NEMS, but since there is no physical implementation in the no NEMS case, the classification task becomes easier for the algorithm.

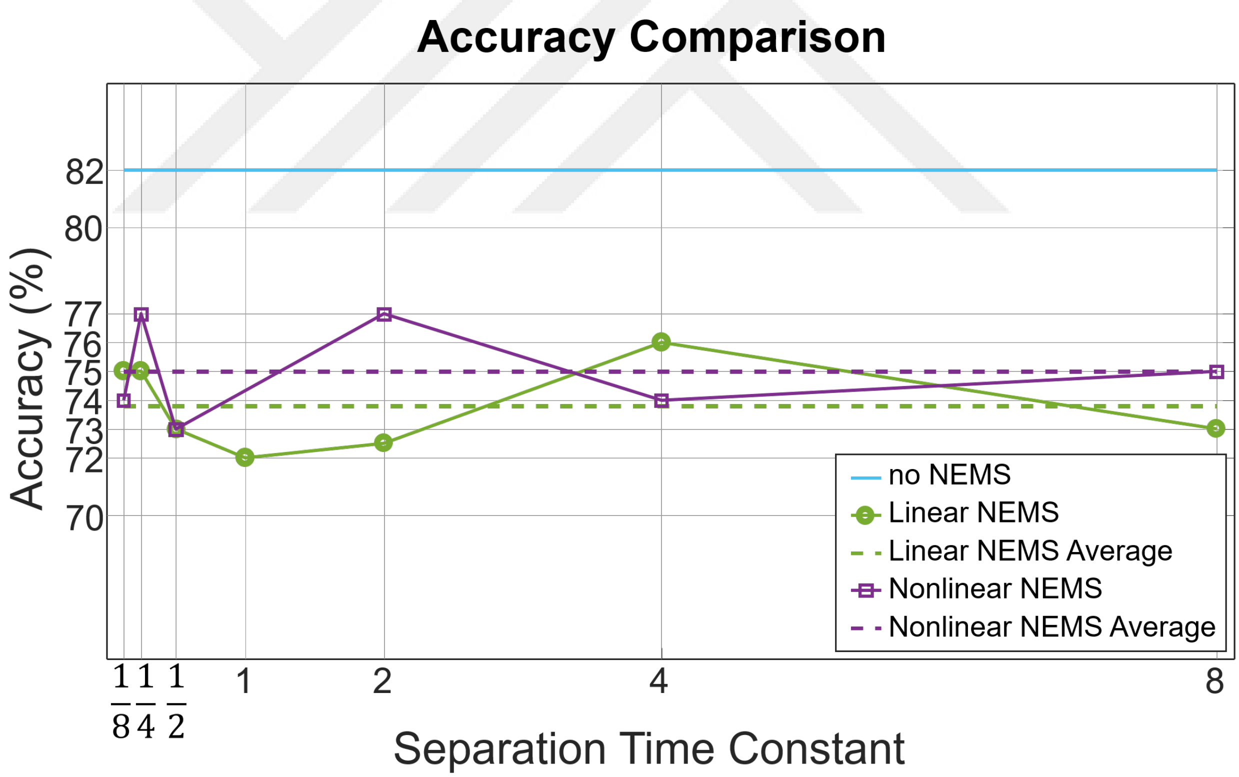

Figure 4.6: Effect of the separation time with paddle NEMS resonator. The comparison of the obtained average accuracy values based on the separation time. The test conditions are: $Q = 58$, $f_{d,linear} = 8.04\,MHz$, $V_{AC,linear} = 400\,mV$; $f_{d,nonlinear} = 8.07\,MHz$, $V_{AC,nonlinear} = 700\,mV$, $V_{DC} = 1\,V$, $T = 14.42\,\mu s$.

As can be seen in Figures 4.6 and 4.7, the average signal-to-noise ratio (SNR) of the nonlinear NEMS is 58% higher than that of the linear NEMS, whereas the average accuracy achieved with nonlinear NEMS is only 1.6% higher than that of the linear NEMS. The correlation coefficient between the SNR and accuracy values is calculated as -0.3 for the experiments conducted with linear NEMS and 0.1 for the ones with nonlinear NEMS. These values indicate a weak relationship between those parameters. Hence, despite the much greater SNR in the nonlinear regime compared to the linear regime of the NEMS, no discernible difference has been observed in the accuracy results. This situation suggests that there are other factors with a greater effect on the accuracy variations between the linear and nonlinear regimes, possibly related to the design or operation of the RC system. The correlation between the SNR and accuracy values could be explored further by cautiously testing higher driving amplitudes to compare the influence of the nonlinearity in the system.

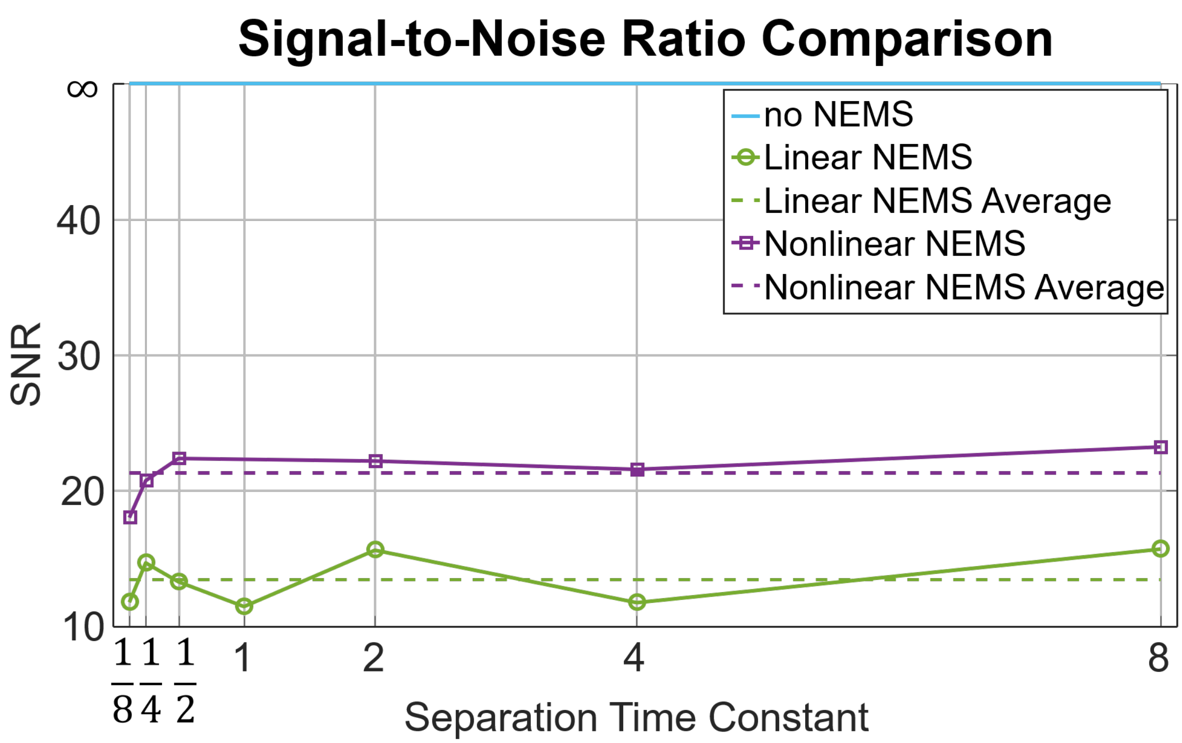

Figure 4.7: Signal-to-noise ratio comparison of the experiments conducted with paddle NEMS resonator.

4.4 Training and Validation Algorithm for the Reservoir Outputs

The algorithm is written using MATLAB software; the code used can be seen in Appendix B. The algorithm starts by importing the required data and setting the variables used in the algorithm. These variables include the pixel number (440), the number of training samples (900), the number of testing samples (100), and the number of data points used at the beginning of the 1000 image data. This is done to distinguish the beginning and end of the data during experiments, as the data collection process takes only seconds, and it can be challenging to visually identify the beginning and end of the data. A dataset of 3000 data points comprising 1000 instances of the value 1, 1000 instances of value 0, and 1000 more instances of value 1 is utilized for this purpose. As a result, the dataset provided to the reservoir consists of 443000 data points $(440\,pixels\ x\ 1000\,images\ +\ 3000\,datapoints\ at\ the\ beginning)$.

Then the *csv* file containing the input data used in the amplitude modulation and the *txt* file with the output of the NEMS reservoir are loaded in the code, along with the *mat* files containing the train and test samples obtained from the MNIST handwritten digit dataset.

The imported input and output data undergo transformations to ensure compatibility during training. Subsequently, the output data is checked to see if any distortion is present. Afterward, the ring-down time value of the resonator, the separation time constant, and the sampling rate utilized in the experiment are inputted in the code. Next, the input and output signals are visualized in the Signal Analyzer application of the MATLAB software to align the data on top of each other for training. The 3000 data points (1-0-1) at the beginning of the input and output data are also valuable in this task. For this, the shifts in input and output timescales are calculated and compensated for data alignment. Once the alignment is completed, the output data is downsampled to match the number of data points in the input data, employing the separation time used in the experiment.

Later, the first 3000 data points are removed from the downsampled output data, followed by the normalization of the output. Then, the resulting data consisting of 440000 data points is converted into a 440x1000 matrix, representing 1000 images with 440 pixels. Now, the images from the NEMS reservoir output are ready to be trained after the images imported from the MNIST dataset are cropped for compatibility. The rest of the code carries out the training and validation processes, elaborated upon in the following sections.

4.4.1 Training with Ridge Regression

This study utilizes the unique nonlinear characteristics of the NEMS resonator employed in the proposed RC architecture to map the input data into a higher dimensional space for using linear regression for the classification of MNIST handwritten digits. The mapping process efficiently converts the complex, multi-dimensional data into a representation that can be linearly separable. The training algorithm for classification uses the advantages of linear regression, such as its simplicity in application and low-cost computation.

However, the linear regression model has the possibility of overfitting, although the NEMS resonator successfully maps the input data. In order to avoid this risk and improve the model, ridge regression is utilized. Ridge regression incorporates a regularization coefficient into the least squares method employed in regular linear regression. The penalty term coming with the regularization coefficient hinders the model from assigning large weights to some aspects of the input data. Thus, it constrains the model from overfitting to the training data and minimizes its variance by penalizing large weights.

The mathematical representation of this algorithm is shown in Equation 4.1.

$$\hat{y} = \mathbf{x}^T \hat{\beta}, \qquad \hat{\beta} = (\mathbf{X}^T\mathbf{X} + \lambda\mathbf{I})^{-1}\mathbf{X}^T\mathbf{y} \tag{4.1}$$

where $\mathbf{y}$ is the actual output, $\hat{y}$ is the guessed output, $\mathbf{X}$ is the matrix consisting of all the input data ($\mathbf{x}$), λ is the regularization coefficient, and $\hat{\beta}$ represents the weights.

While employing the ridge regression in the training algorithm, a custom function is written that calculates the weights. The function begins by generating a $10x900$ regression matrix representing the 10-digit classes and 900 training images to become a one-hot representation of the trained data later in a for loop. Then, another matrix with dimensions of $10x440$ representing the 10-digit classes and 440 pixels is built to store the weights in the same for loop. Finally, in the for loop, the regression matrix is filled to create a one-hot representation of the trained data, and the weights matrix is filled with the values calculated using MATLAB's built-in *ridge* function, taking the regression matrix and trained data matrix with the optimal regularization coefficient determined through the mentioned search process as inputs.

The choice of the regularization coefficient, represented by λ, is crucial in achieving optimal performance using ridge regression. A smaller value of λ reduces the influence of the penalty term, causing the model to work like regular linear regression. On the contrary, large values of λ eliminate large coefficients too much, creating a potential risk of underfitting. A careful search procedure is utilized to determine the ideal value of λ that minimizes the total error on a specified validation set in the training algorithm. A delicate balance between model complexity and performance is achieved by integrating ridge regression and neatly choosing the regularization coefficient. As a result, a more practical algorithm is created for the MNIST handwritten digits classification task in this study.

4.4.2 K-fold Validation

When evaluating the classification performance of the proposed single nonlinear NEMS resonator RC system, the k-fold validation method is considered to be the most appropriate approach. The validation is conducted with 600 randomized folds to guarantee that it is carried out fairly. The validation sets have been created using 100 digits. However, when this was done by selecting 100 consecutive digits from the main dataset of 1000, it resulted in the validation data having different numbers of digits from different digit classes. This situation results in an undesired biased calculation.

In order to address this issue, a validation fold consisting of 100 digits, including 10 digits from each digit class, has been created, ensuring that the effect of each of the 10 classes (0-9) is evenly represented. Yet, selecting 10 digits from each class has the potential to introduce bias due to the presence of several potential combinations. Hence, the digits were randomly selected 600 times, and the resulting accuracies were averaged to get the reported accuracies in this thesis. This is accomplished by providing 600 different seeds to the *random number generator* is the code.

Chapter 5

Conclusion and Future Remarks

In this work, a simplified single nonlinear NEMS resonator RC system operating at ambient pressure with its intrinsic nonlinear dynamics is presented. Compared to the state-of-the-art with significantly higher ring-down times, the proposed system avoids the need for complex vacuum setups and offers more efficient and faster information processing. Furthermore, the experiments with the NEMS reservoir can be completed within minutes owing to its high processing speed, while it can be integrated into various systems due to its small size. As a result, the proposed novel RC system offers a practical and broadly applicable alternative to the traditional RC systems thanks to the improved system parameters, particularly lower decay times. A comparison between classification speeds of other RC works is displayed in Table 5.1.

The proposed single nonlinear nanoelectromechanical resonator reservoir computing model, in light of the findings of this study, offers several advantages. These include the ability to operate in atmospheric conditions, rapid operation speed due to the low ring-down times of the resonator, and portability and applicability due to its compact size. Nevertheless, it is recommended to investigate a broader spectrum of separation times in order to improve the capabilities of the proposed model. This allows for additional adjustments to be made to the NEMS reservoir's nonlinearity and memory capacity. Moreover, conducting experiments and training with a dataset consisting of more than 1000 images will enhance the comprehensiveness of the model in evaluating the classification accuracy of the NEMS reservoir. Furthermore, trying different device designs to manipulate the quality factor and fundamental frequency of the device could allow control over the resonator ring-down time and, thus, the experiment parameters. Also, the devices and experiments should be designed further to reach higher nonlinear driving amplitudes. Finally, as this study only evaluates the MNIST handwritten digit recognition benchmark, it would be beneficial to evaluate the proposed architecture in more relevant and challenging applications.

Reference	Publication Year	Technology	Ring-down/Relaxation Time
[8]	2021	MEMS Resonator	∼16 milliseconds
[9]	2021	MEMS Resonator	few microseconds
[22]	2021	MEMS Resonator	∼330 microseconds
[23]	2020	MEMS Resonator	∼96 microseconds
[24]	2022	Photo-Synaptic Memristor Array	29 - 280 milliseconds
[25]	2022	3D Memristor	∼600 microseconds
[26]	2022	3D Dynamic Memristor Array	few microseconds
[7]	2021	2D Memristor	∼100 milliseconds
[6]	2021	Dynamic Memristor	∼400 microseconds
[27]	2020	Memristor Network	∼100 milliseconds
[28]	2019	Magnetic Skyrmion Memristor	∼25 nanoseconds
[29]	2022	Optoelectronic Synapse on Van der Waals layer	30 - 900 milliseconds
[30]	2021	Biocompatible Organic Electrochemical Network	∼100 milliseconds
[31]	2023	Ferroelectrics	12 - 280 milliseconds
[32]	2022	Ferroelectric FET	∼100 nanoseconds
[33]	2021	Photonics	range of picoseconds to microseconds
[34]	2021	Spin-torque Nano-oscillator	∼200 nanoseconds
[35]	2021	Spintronics	10 - 100 nanoseconds
[36]	2020	Spintronics	hundreds of nanoseconds
[37]	2019	Spin-torque Nano-oscillator	∼4 nanoseconds
[38]	2021	Stripe Magnetic Garnet	few nanoseconds

Table 5.1: A Comparison of Recent Reservoir Computing Speeds

Bibliography

[1] D. Verstraeten, B. Schrauwen, M. d'Haene, and S. D., "An experimental unification of reservoir computing methods," *Neural Networks*, vol. 20, no. 3, pp. 391–403, 2007.

[2] H. Jaeger, "The "echo state" approach to analysing and training recurrent neural networks-with an erratum note," Tech. Rep. 34, Bonn, Germany: German National Research Center for Information Technology GMD Technical Report, 2001.

[3] W. Maass, T. Natschläger, and H. Markram, "Real-time computing without stable states: A new framework for neural computation based on perturbations," *Neural Computation*, vol. 14, no. 11, pp. 2531–2560, 2002.

[4] X. Liang, J. Tang, Y. Zhong, B. Gao, H. Qian, and H. Wu, "Physical reservoir computing with emerging electronics," *Nature Electronics*, pp. 1–14, 2024.

[5] S. Kokalj-Filipovic, P. Toliver, W. Johnson, and R. Miller, "Reservoir-based distributed machine learning for edge operation," *arXiv preprint arXiv:2104.00751*, 2021.

[6] Y. Zhong, J. Tang, X. Li, B. Gao, H. Qian, and H. Wu, "Dynamic memristor-based reservoir computing for high-efficiency temporal signal processing," *Nature Communications*, vol. 12, no. 1, p. 408, 2021.

[7] L. Sun *et al.*, "In-sensor reservoir computing for language learning via two-dimensional memristor," *Science Advances*, vol. 7, no. 20, p. eabg1455, 2021.

[8] J. Sun *et al.*, "Novel nondelay-based reservoir computing with a single micromechanical nonlinear resonator for high-efficiency information processing," *Microsystems & Nanoengineering*, vol. 7, no. 1, p. 83, 2021.

[9] T. Zheng *et al.*, "Enhancing performance of reservoir computing system based on coupled mems resonators," *Sensors*, vol. 21, no. 9, p. 2961, 2021.

[10] I. Bargatin, I. Kozinsky, and R. M., "Efficient electrothermal actuation of multiple modes of high-frequency nanoelectromechanical resonators," *Applied Physics Letters*, vol. 90, no. 9, p. 093116, 2007.

[11] A. B. Arı, "Design, fabrication, and applications of multi-mode nanoelectromechanical systems," Master's thesis, Bilkent University, Türkiye, 2017.

[12] R. T. Erdoğan, "Sensing and characterization of single nanoparticles by vacuum-free nanoelectromechanical systems with an integrated polymeric lens," Master's thesis, Bilkent University, Türkiye, 2021.

[13] B. E. Kaynak, "Towards mode shape independent nanoelectromechanical mass spectrometry under atmospheric conditions," Master's thesis, Bilkent University, Türkiye, 2023.

[14] R. T. Erdogan, M. Alkhaled, B. E. Kaynak, H. Alhmoud, H. S. Pisheh, M. Kelleci, I. Karakurt, C. Yanik, Z. B. Şen, B. Sari, A. M. Yagci, A. Özkul, and M. S. Hanay, "Atmospheric pressure mass spectrometry of single viruses and nanoparticles by nanoelectromechanical systems," *ACS Nano*, vol. 16, no. 3, pp. 3821–3833, 2022.

[15] A. B. Arı, M. C. Karakan, C. Yanik, İ. İ. Kaya, and M. S. Hanay, "Intermodal coupling as a probe for detecting nanomechanical modes," *Physical Review Applied*, vol. 9, no. 3, p. 034024, 2018.

[16] M. Li, H. X. Tang, and M. L. Roukes, "Ultra-sensitive nems-based cantilevers for sensing, scanned probe and very high frequency applications," *Nature Nanotechnology*, vol. 2, no. 2, pp. 114–120, 2007.

[17] C. Ti, A. B. Arı, M. C. Karakan, C. Yanik, İ. İ. Kaya, M. S. Hanay, O. Svitelskiy, M. González, H. Seren, and K. L. Ekinci, "Frequency-dependent

piezoresistive effect in top-down fabricated gold nanoresistors," *Nano Letters*, vol. 21, no. 15, pp. 6533–6539, 2021.

[18] M. Sansa, M. Fernández-Regúlez, J. Llobet, Á. San Paulo, and F. Pérez-Murano, "High-sensitivity linear piezoresistive transduction for nanomechanical beam resonators," *Nature Communications*, vol. 5, no. 1, p. 4313, 2014.

[19] T. Kouh, M. S. Hanay, and K. L. Ekinci, "Nanomechanical motion transducers for miniaturized mechanical systems," *Micromachines*, vol. 8, no. 4, p. 108, 2017.

[20] M. Yuksel, E. Orhan, C. Yanik, A. B. Ari, A. Demir, and M. S. Hanay, "Nonlinear nanomechanical mass spectrometry at the single-nanoparticle level," *Nano Letters*, vol. 19, no. 6, pp. 3583–3589, 2019.

[21] B. E. Kaynak, M. Alkhaled, E. Kartal, C. Yanik, and M. S. Hanay, "Atmospheric-pressure mass spectrometry by single-mode nanoelectromechanical systems," *Nano Letters*, vol. 23, no. 18, pp. 8553–8559, 2023.

[22] G. Dion, A. I.-E. Oudrhiri, B. Barazani, A. Tessier-Poirier, and J. Sylvestre, *Reservoir Computing: Theory, Physical Implementations, and Applications*, ch. Reservoir Computing in MEMS, pp. 191–217. K. Nakajima and I. Fischer Eds. Singapore: Springer Singapore, 2021.

[23] B. Barazani, G. Dion, J.-F. Morissette, L. Beaudoin, and J. Sylvestre, "Microfabricated neuroaccelerometer: integrating sensing and reservoir computing in mems," *Journal of Microelectromechanical Systems*, vol. 29, no. 3, pp. 338–347, 2020.

[24] Z. Zhang *et al.*, "In-sensor reservoir computing system for latent fingerprint recognition with deep ultraviolet photo-synapses and memristor array," *Nature Communications*, vol. 13, no. 1, p. 6590, 2022.

[25] A. H. Jaafar *et al.*, "3d-structured mesoporous silica memristors for neuromorphic switching and reservoir computing," *Nanoscale*, vol. 14, no. 46, pp. 17170–17181, 2022.

[26] W. Sun *et al.*, "3d reservoir computing with high area efficiency (5.12 tops/mm^2 implemented by 3d dynamic memristor array for temporal signal processing," in *2022 IEEE Symposium on VLSI Technology and Circuits (VLSI Technology and Circuits), 12-17 June 2022*, pp. 222–223, 2022.

[27] X. Zhu, Q. Wang, and W. D. Lu, "Memristor networks for real-time neural activity analysis," *Nature Communications*, vol. 11, no. 1, p. 2439, 2020.

[28] W. Jiang *et al.*, "Physical reservoir computing using magnetic skyrmion memristor and spin torque nano-oscillator," *Applied Physics Letter*, vol. 115, no. 19, 2019.

[29] K. Liu *et al.*, "An optoelectronic synapse based on $\alpha - in_2se_3$ with controllable temporal dynamics for multimode and multiscale reservoir computing," *Nature Electronics*, vol. 5, no. 11, pp. 761–773, 2022.

[30] M. Cucchi, C. Gruener, L. Petrauskas, P. Steiner, H. Tseng, and A. Fischer, "Reservoir computing with biocompatible organic electrochemical networks for brain-inspired biosignal classification," *Science Advances*, vol. 7, no. 34, p. eabh0693, 2021.

[31] Z. Chen *et al.*, "All-ferroelectric implementation of reservoir computing," *Nature Communications*, vol. 14, no. 1, p. 3585, 2023.

[32] M. Tang *et al.*, "A compact fully ferroelectric-fets reservoir computing network with sub-100 ns operating speed," *IEEE Electron Device Letters*, vol. 43, no. 9, pp. 1555–1558, 2022.

[33] K. Kanno and A. Uchida, *Reservoir Computing: Theory, Physical Implementations, and Applications*, ch. Performance improvement of delay-based photonic reservoir computing, pp. 377–396. K. Nakajima and I. Fischer Eds. Singapore: Springer Singapore, 2021.

[34] M. Riou *et al.*, *Reservoir Computing: Theory, Physical Implementations, and Applications*, ch. Reservoir computing leveraging the transient non-linear dynamics of spin-torque nano-oscillators, pp. 307–329. K. Nakajima and I. Fischer Eds. Singapore: Springer Singapore, 2021.

[35] T. Taniguchi, S. Tsunegi, S. Miwa, K. Fujii, H. Kubota, and K. Nakajima, *Reservoir Computing: Theory, Physical Implementations, and Applications*, ch. Reservoir Computing Based on Spintronics Technology, pp. 331–360. K. Nakajima and I. Fischer Eds. Singapore: Springer Singapore, 2021.

[36] N. Akashi *et al.*, "Input-driven bifurcations and information processing capacity in spintronics reservoirs," *Physical Review Research*, vol. 2, no. 4, p. 043303, 2020.

[37] D. Marković *et al.*, "Reservoir computing with the frequency, phase, and amplitude of spin-torque nano-oscillators," *Applied Physics Letters*, vol. 114, no. 1, 2019.

[38] R. Nakane, A. Hirose, and G. Tanaka, "Spin waves propagating through a stripe magnetic domain structure and their applications to reservoir computing," *Physical Review Research*, vol. 3, no. 33, p. 033243, 2021.

[39] A. K. Naik, M. S. Hanay, W. K. Hiebert, X. L. Feng, and M. L. Roukes, "Towards single-molecule nanomechanical mass spectrometry," *Nature Nanotechnology*, vol. 4, no. 7, pp. 445–450, 2009.

[40] J. B. Fenn, M. Mann, C. K. Meng, S. F. Wong, and C. M. Whitehouse, "Electrospray ionization for mass spectrometry of large biomolecules," *Science*, vol. 246, no. 4926, pp. 64–71, 1989.

[41] S. D. Fuerstenau, W. H. Benner, J. J. Thomas, C. Brugidou, B. Bothner, and G. Siuzdak, "Mass spectrometry of an intact virus," *Angewandte Chemie*, vol. 113, no. 3, pp. 559–562, 2001.

[42] T. Doussineau, C. Y. Bao, R. Antoine, P. Dugourd, W. Zhang, F. d'Agosto, and B. Charleux, "Direct molar mass determination of self-assembled amphiphilic block copolymer nanoobjects using electrospray-charge detection mass spectrometry," *ACS Macro Letters*, vol. 1, no. 3, pp. 414–417, 2012.

[43] C. Comby-Zerbino, X. Dagany, F. Chirot, P. Dugourd, and R. Antoine, "The emergence of mass spectrometry for characterizing nanomaterials. atomically precise nanoclusters and beyond," *Materials Advances*, vol. 2, no. 4896, 2021.

[44] M. S. Hanay, S. Kelber, A. K. Naik, D. Chi, S. Hentz, E. C. Bullard, E. Colinet, L. Duraffourg, and M. L. Roukes, "Single-protein nanomechanical mass spectrometry in real time," *Nature Nanotechnology*, vol. 7, no. 9, pp. 602–608, 2012.

[45] O. Malvar, J. J. Ruz, P. M. Kosaka, C. M. Dominguez, E. Gil-Santos, M. Calleja, and J. Tamayo, "Mass and stiffness spectrometry of nanoparticles and whole intact bacteria by multimode nanomechanical resonators," *Nature Communications*, vol. 7, no. 1, p. 13452, 2016.

[46] S. Dominguez-Medina, S. Fostner, M. Defoort, M. Sansa, A. K. Stark, M. A. Halim, E. Vernhes, M. Gely, G. Jourdan, T. Alava, P. Boulanger, C. Masselon, and S. Hentz, "Neutral mass spectrometry of virus capsids above 100 megadaltons with nanomechanical resonators," *Science*, vol. 362, no. 6417, pp. 918–922, 2018.

[47] S. Dohn, W. Svendsen, A. Boisen, and O. Hansen, "Mass and position determination of attached particles on cantilever based mass sensors," *Review of Scientific Instruments*, vol. 78, no. 10, p. 103303, 2007.

[48] M. K. Ghatkesar, V. Barwich, T. Braun, J. P. Ramseyer, C. Gerber, M. Hegner, H. P. Lang, U. Drechsler, and M. Despont, "Higher modes of vibration increase mass sensitivity in nanomechanical microcantilevers," *Nanoetchnology*, vol. 18, no. 44, p. 445502, 2007.

[49] M. S. Hanay, S. I. Kelber, C. D. O'Connell, P. Mulvaney, J. E. Sader, and M. L. Roukes, "Inertial imaging with nanomechanical systems," *Nature Nanotechnology*, vol. 10, no. 4, pp. 339–344, 2015.

Appendix A

Fabrication of NEMS Devices

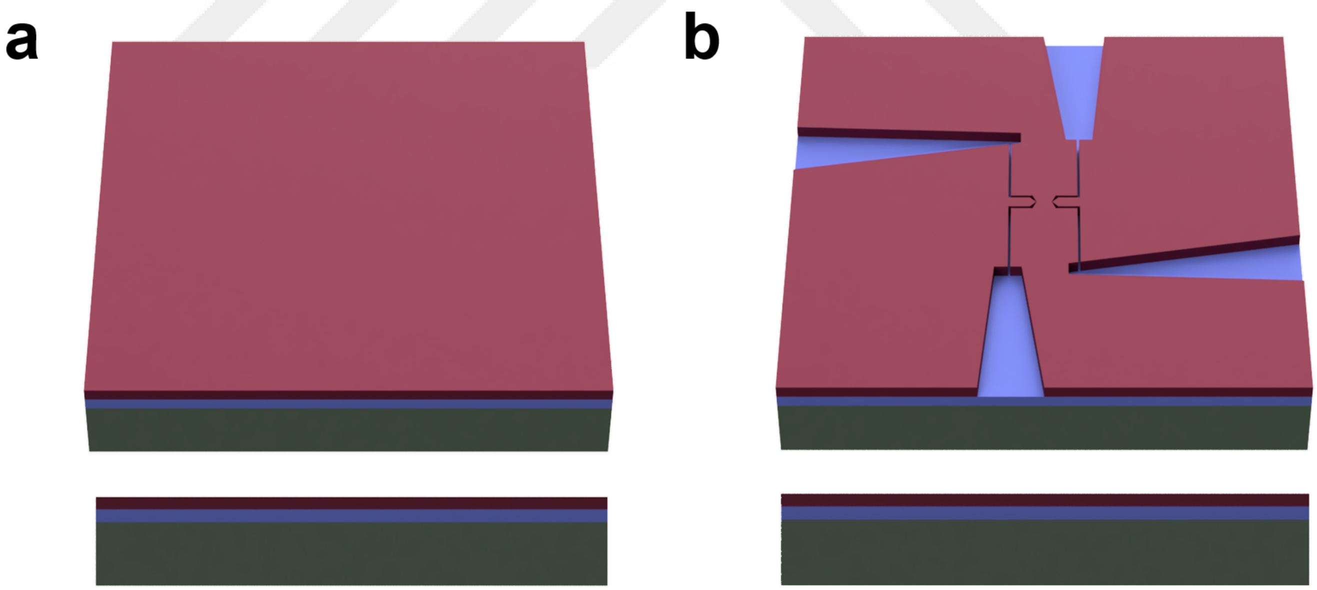

Figure A.1: **(a)** Top/front & section view: Sample after the first bilayer PMMA coating. **(b)** Top/front & section view: Sample after the first EBL step for patterning the gold regions and development.

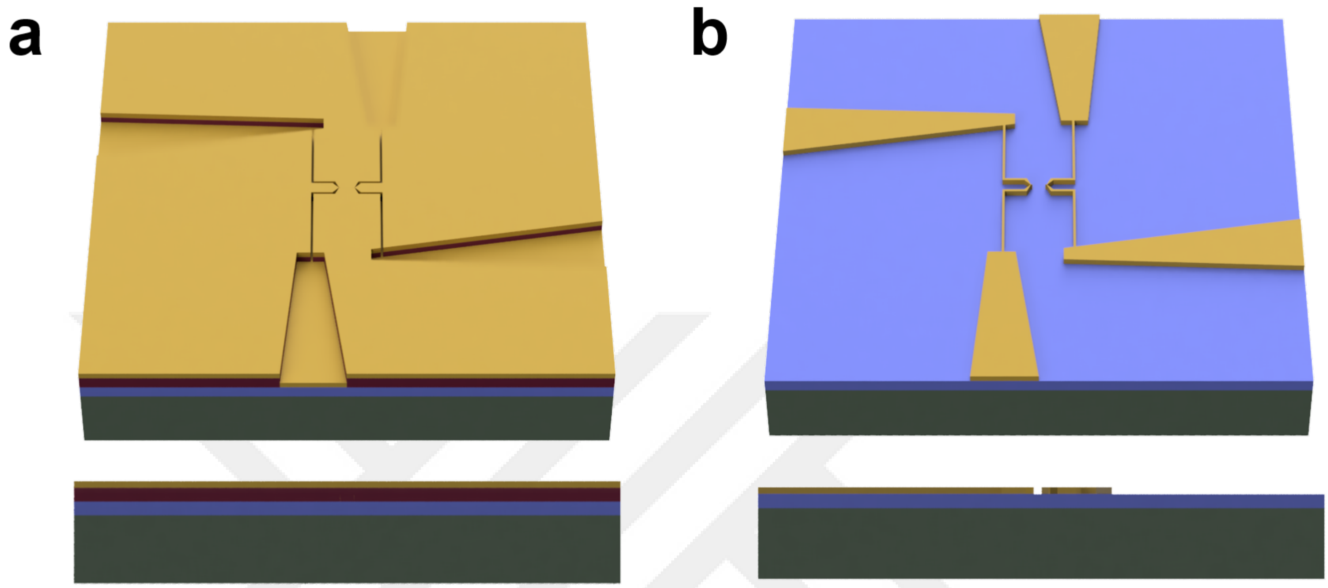

Figure A.2: **(a)** Top/front & section view: Sample after the chromium and gold deposition. **(b)** Top/front & section view: Sample after the first lift-off.

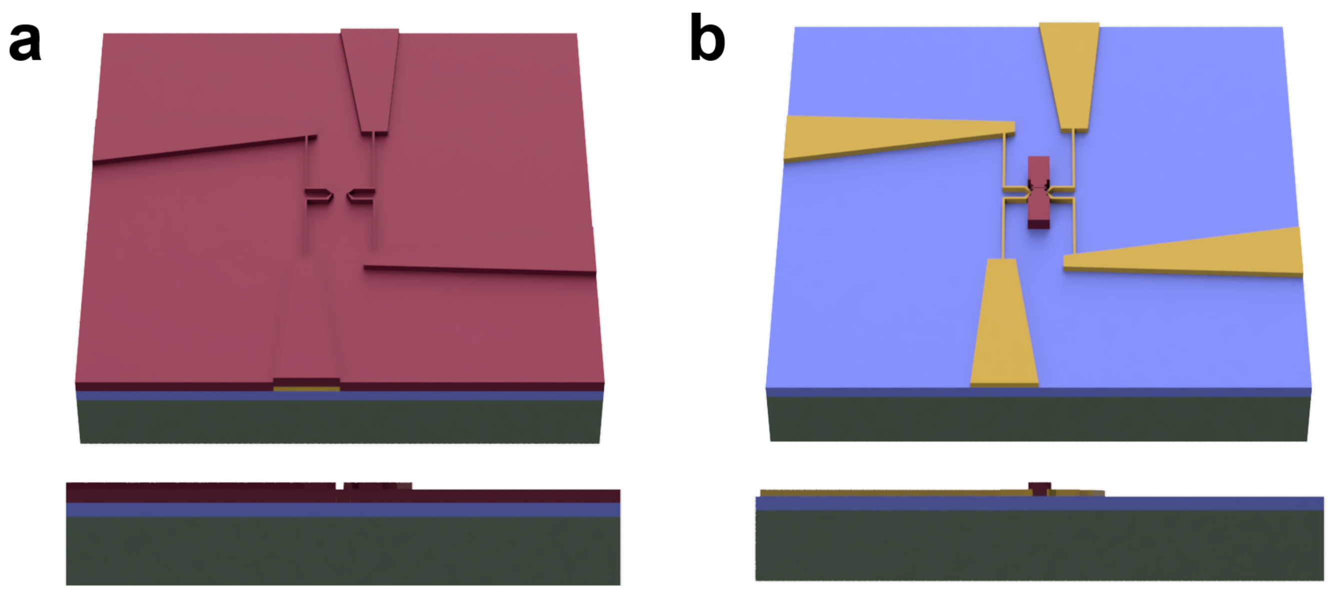

Figure A.3: **(a)** Top/front & section view: Sample after the second bilayer PMMA coating. **(b)** Top/front & section view: Sample after the second EBL step for patterning the copper etch mask and development.

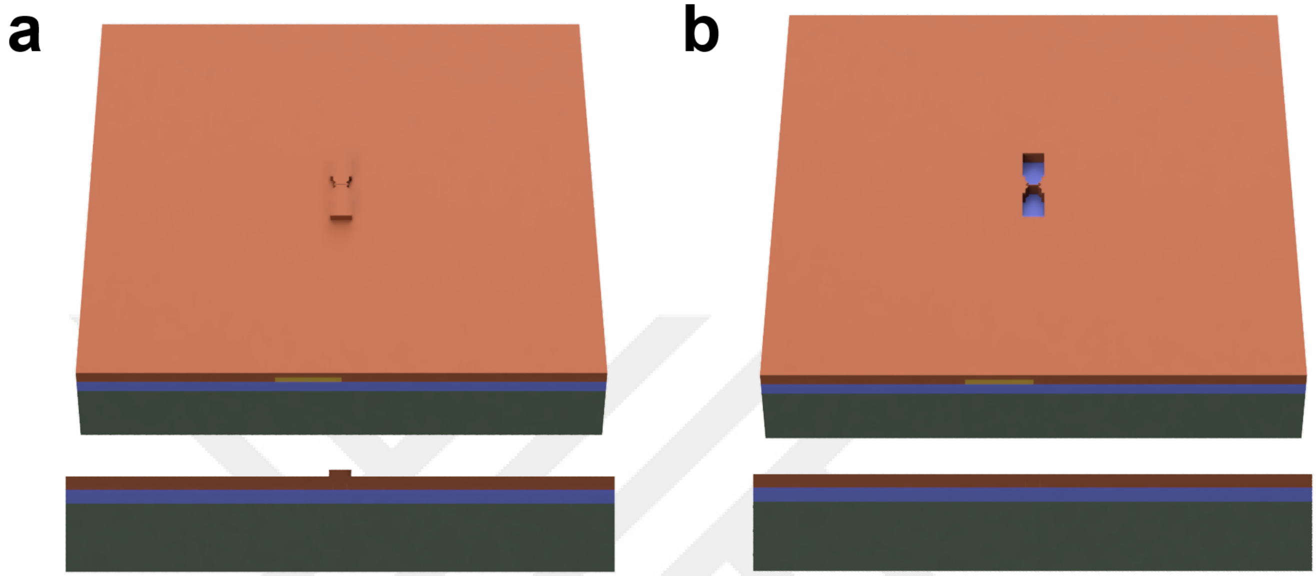

Figure A.4: **(a)** Top/front & section view: Sample after the copper deposition. **(b)** Top/front & section view: Sample after the second lift-off.

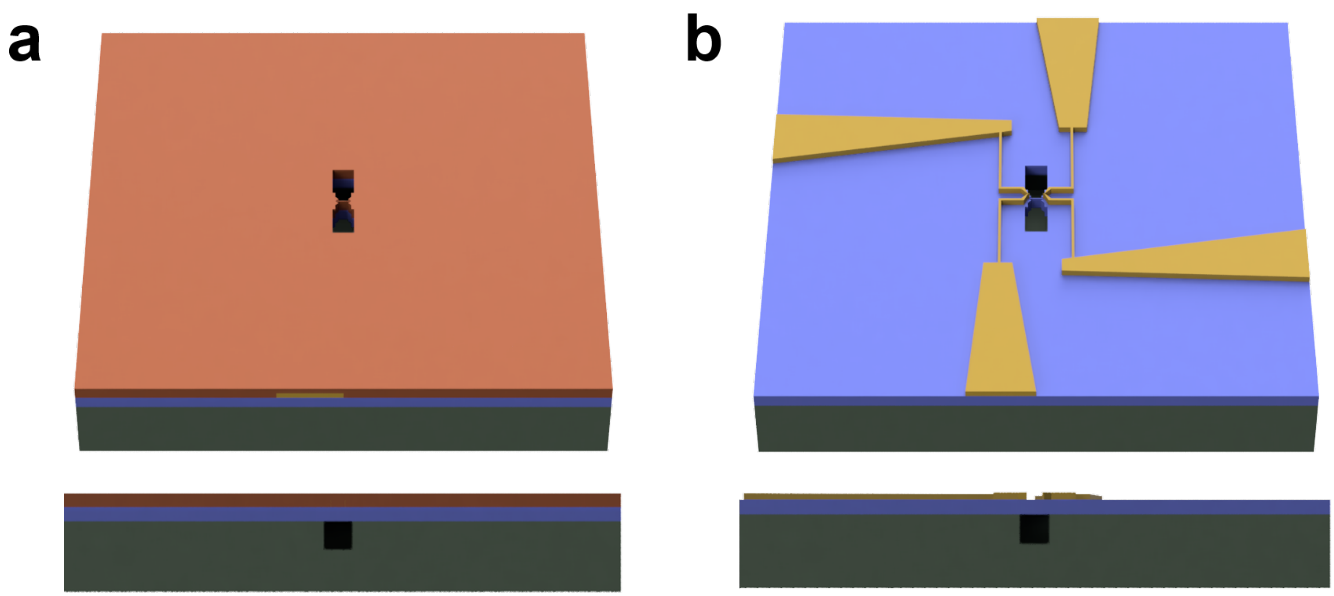

Figure A.5: **(a)** Top/front & section view: Sample after the anisotropic silicon nitride etching and isotropic nitride etching using ICP to suspend the beam structure. **(b)** Top/front & section view: Sample after the copper etch mask removal.

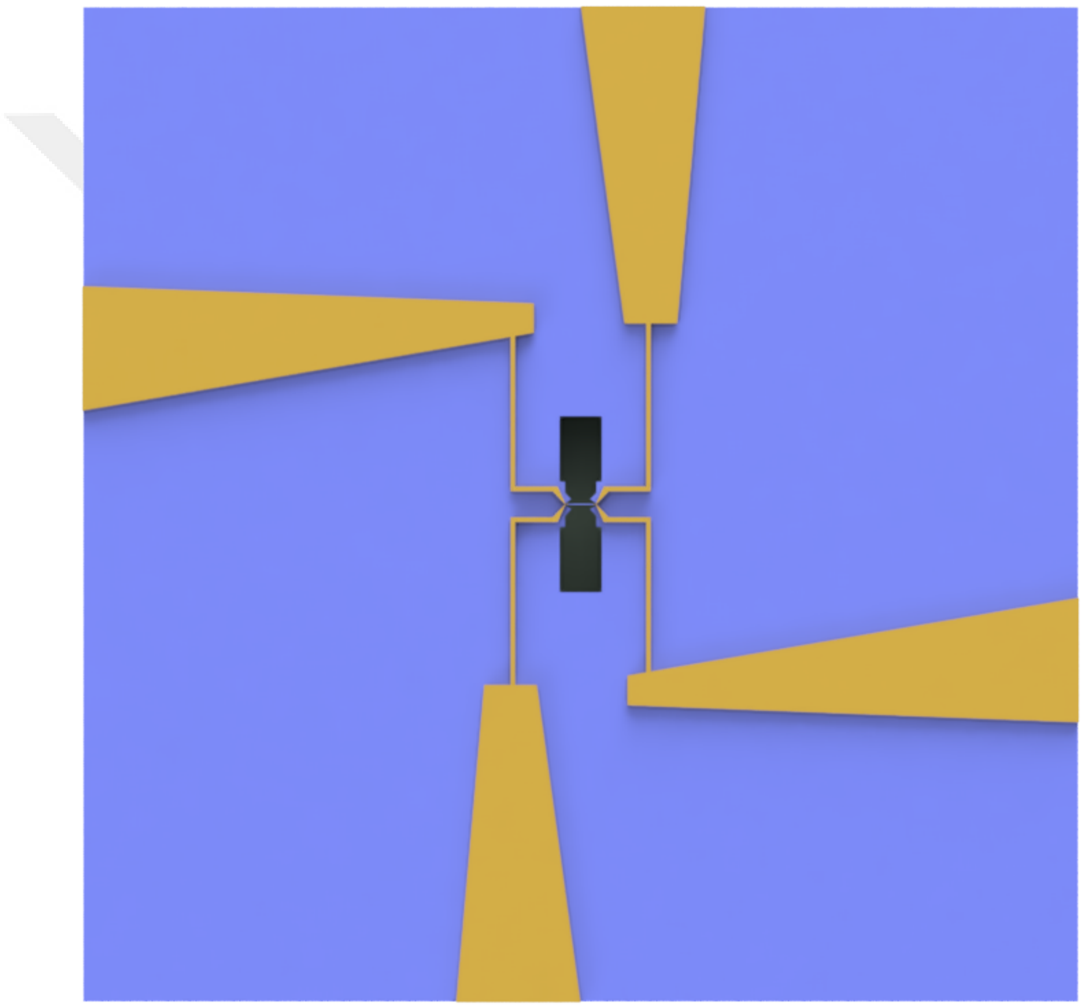

Figure A.6: Final view of the NEMS chip (top). The device is ready to be placed on a custom PCB, wire-bonded, and used in the experiments.

Appendix B

MATLAB Code for Training and Validation of the Reservoir Outputs

```
close all; clear; clc;

%% Importing the Data & Setting the Variables

pixels = 440; % pixel number for each image
num_train = 900; % number of train images
num_test = 100; % number of test images
num_image = num_train + num_test; % total number of images
beg_data = 3000; % number of data in the beginning
num_data = pixels*num_image + beg_data; % total number of data

in_file = 'ae.csv'; % input file name
out_file = 'paper_data_020922_08.txt'; % output file name
test_file = 'test_samples.mat'; % test images
train_file = 'train_samples.mat'; % train images
```

```
    filename = out_file; % output file name
    fid = fopen(filename); % open the output file
    % get the amplitude and time data
    data = textscan(fid, '%f %f','Delimiter',';','headerlines',5);

    r_temp = data{2}; % output amplitude
    t_temp = data{1}; % output time

    input = readmatrix(in_file); % read given data
    input = input(1:num_data); % in case of eliminating images
    input = (input./2+(1/2)).^2; % since the input is 2*sqrt()-1, reverse it

    % remove the distorted data
    dist_ind = [];

    for i = 2:length(r_temp)
        if t_temp(i)-t_temp(i-1) > 1e-4
            dist_ind = [dist_ind i];
        end
    end

    ring_down_t = 6.25e-6; % ring down time
    sep_t_coef = 0.8; % seperation time calculation coefficient
    samp_rate = 460.6e3; % sampling rate

    shift_in_per = -2.6e-3-10.8e-6; % shift in input period
    shift_out_t = 15.249707+5e-3-2.5e-6-2*(2.2123892); % shift in output time

    % calculate delayed time, checking from signal analyser
```

```
    delayed_t = num_data*ring_down_t*sep_t_coef + shift_in_per;
    % using the calculated time, construct input time
    t_input = linspace(0,delayed_t,length(input))';

    t = t_temp + shift_out_t; % shift the output time since it starts late
    r = r_temp./max(r_temp); % normalise the amplitude

    %% Downsampling the Output

    ind = zeros(1,num_data); % initialise index array
    % get the first index of the output time when it is equal to the input time
    ind(1) = find(t-t_input(1)<1e-6,1,'last');

    shift_samp_per = -2.96e-3; % shift in sampling period

    % calculate the sampling period, checking from signal analyser
    samp_period = (num_data*ring_down_t*sep_t_coef+shift_samp_per)/...
        (num_data*sep_t_coef);
    jump = samp_period*samp_rate*sep_t_coef; % jump between each signal

    % get the remaining indices for the output time
    for i = 2:num_data
        ind(i) = ind(1)+jump*(i-1);
    end

    ind2down = round(ind); % round the indices to use
    r_downsampled = r(ind2down); % get the undersampled amplitude
```

```
%% Getting the Images

ind2tr = round(ind); % indices to train the data (one
    seperation time)
r_train = r(ind2tr); % amplitudes to train the data

r_train = r_train(beg_data+1:end); % remove the data in the
     beginning

for j=1:num_image
    r_train(pixels*(j-1)+1:pixels*j) = r_train(pixels*(j-1)
        +1:pixels*j)/...
         sum(r_train(pixels*(j-1)+1:pixels*j));
end

exp_020922_08 = r_train;

save("exp_020922_08.mat",'exp_020922_08')

% reshape the data to train in pixels x train data number
    matrices
x_tr = reshape(r_train(num_test*pixels+1:end),[pixels
    num_train])'; % first 100 test

% reshape the data to train in pixels x test data number
    matrices
x_te = reshape(r_train(1:num_test*pixels),[pixels num_test
    ])'; % first 100 test

x = [x_te;x_tr];

%% Loading the Images
```

```

load(test_file) % load the test images
load(train_file) % load the train images

%% Training & Validation

total = vertcat(train,test); % total dataset
acc = zeros(1,600);

for n = 250001:200:370000

    rng(n) % seed the random number generator

    y = total(:,1); % get the correct digits
    idxMAT = zeros(10,10); % initialize the random indices
      matrix

    for i=0:9 % for each digit
        idx_dgt = find(y == i); % find the indices of each
          digit
        % get 10 random numbers for that digit
        rndm_idx_dgt = randperm(length(idx_dgt),10);
        % choose digits of the random indices
        rndm_chosen_dgt = idx_dgt(rndm_idx_dgt); % place in
          the matrix
        idxMAT(i+1,:) = rndm_chosen_dgt;
    end
    idxVect = reshape(idxMAT,[1 100]); % vectorize the
      random indices

    % test data indices from above (10 randomly chosen
      images from each digit)
    idx_test = idxVect;
```

```
        % training data
        idx_train = ~ismember(1:1000,idx_test);

        % construct the random test and train datasets
        test = total(idx_test,:);
        train = total(idx_train,:);

        y_train = train(:,1); % the number shown in each image to train
        x_train_initial = train(:,2:end); % pixels of each image to train (28x28)

        y_test = test(:,1); % the number shown in each image to test
        x_test_initial = test(:,2:end); % pixels of each image to test (28x28)

        y = vertcat(y_train,y_test);

        x_te = x(idx_test,:);
        x_tr = x(idx_train,:);

        % initialise pixels for train images (22x20)
        x_train = zeros(length(y_train),pixels);
        % initialise pixels for test images (22x20)
        x_test = zeros(length(y_test),pixels);

        % crop each image and normalise each pixel
        for i = 1:length(y_train)
            x_train(i,:) = crop(x_train_initial(i,:))/255;
            if i< num_test+1
                x_test(i,:) = crop(x_test_initial(i,:))/255;
            end
```

```
        end

        %% Confusion Matrix and the Accuracy of the Training

        % normalize the output data
        for i=1:num_train
            x_train(i,:)=x_train(i,:)/sum(x_train(i,:));
        end

        for i=1:num_test
            x_test(i,:)=x_test(i,:)/sum(x_test(i,:));
        end

        weights = output_training(y_train,x_tr); % get the weights of train images

        [~,index] = max(weights*x_te',[],1); % guess the test images
        guess = index - 1; % substract 1 to get 0-9 from 1-10

        % get the confusion matrix of the guesses and plot
        C = confusionmat(y_test,guess);

        % cm = confusionchart(C,[0 1 2 3 4 5 6 7 8 9],'RowSummary','row-normalized');
        % cm.Title = 'Confusion Matrix of the Model';

        % sum up the diagonals of the confusion matrix to get the accuracy
        accuracy = sum(diag(C))/length(y_test);
        acc(n) = accuracy;
        % fprintf("Accuracy is: %3.2f \n", accuracy); % announce the accuracy
```

```
    end

    %% Functions Used in Training

    function signal = crop(vector)
    image = reshape(vector,[28, 28]); % reshape the pixels in
      28x28
    c_image = image(4:25,5:24); % crop the image to make it 22
      x20 pixels
    signal = reshape(c_image,[440,1]); % reshape the cropped
      image in 440x1
    end

    function weights = output_training(y_train,x_train)
    y_reg = zeros(10,length(y_train)); % initialise 10 row
      regression matrix
    weights = zeros(10,440); % initialise 10 row weight matrix
    for i = 1:10 % for each image
        % detect the indices of each number shown in the images
            (0 to 9)
        y_reg(i,y_train==i-1) = 1;
        % for each number shown, check its BW values and get
           the weight
        weights(i,:) = ridge(y_reg(i,:)',x_train,400);
    end
    end
```

Appendix C

Mass Spectrometry with Nanoelectromechanical Systems (NEMS)

In literature, these systems have been used for the mass spectrometry (MS) of large particles that are particularly heavier than 10 MDa [39]. However, the capability of measuring such mass range cannot be done by conventional MS systems [40]. The mentioned analytes can be metallic, ceramic, polymeric particles, or organic matter, such as viruses and lipid vesicles; however, none of these analytes can be measured using the commercial MS [41]. One exceptional conventional MS technique, known as charge detection MS (CDMS), can detect analytes within the specified mass range by measuring both the mass-to-charge ratio and the charge at the same time to get the mass value [42]. Nonetheless, the NEMS-MS can measure mass without measuring other analyte properties, which makes the MS dependent on only the mass values and, thus, more reliable than the conventional methods [43]. Additionally, since NEMS are implemented on small chips, they have a smaller footprint, weigh less, and are simpler to deploy in more complicated systems.

C.1 Atmospheric Mass Spectrometry with NEMS

The NEMS-MS works basically by moving the analytes on a resonating nano-beam, with a few micrometers in length and less than a micrometer in width. Since the movement of the particles can result anywhere on the chip, a variety of lensing methods have been developed to focus the particles on the beam, including ion optics, aerodynamic lensing, and electrospray ionization (ESI) techniques [39, 44–46]. Since the ion optics and aerodynamic lensing methods require expensive and complex ultra-high vacuum (UHV) systems, a polymeric lens has been invented to focus the analytes on the beam through the use of ESI and improve the capture efficiency. This lens is essentially a photoresist layer on the NEMS chip with an opening aligned with the beam, and it charges up as the ions generated by ESI move toward the chip. After some time, the lens accumulates enough charge to push the incoming same-charged ions towards the opening, i.e., on the resonator beam. The employment of this system allowed the NEMS-MS experiments to be done under atmospheric conditions, resulting in a six-order-of-magnitude improvement in capture efficiency compared to the previous state-of-the-art with only one-order-of-magnitude decrease in mass resolution [14].

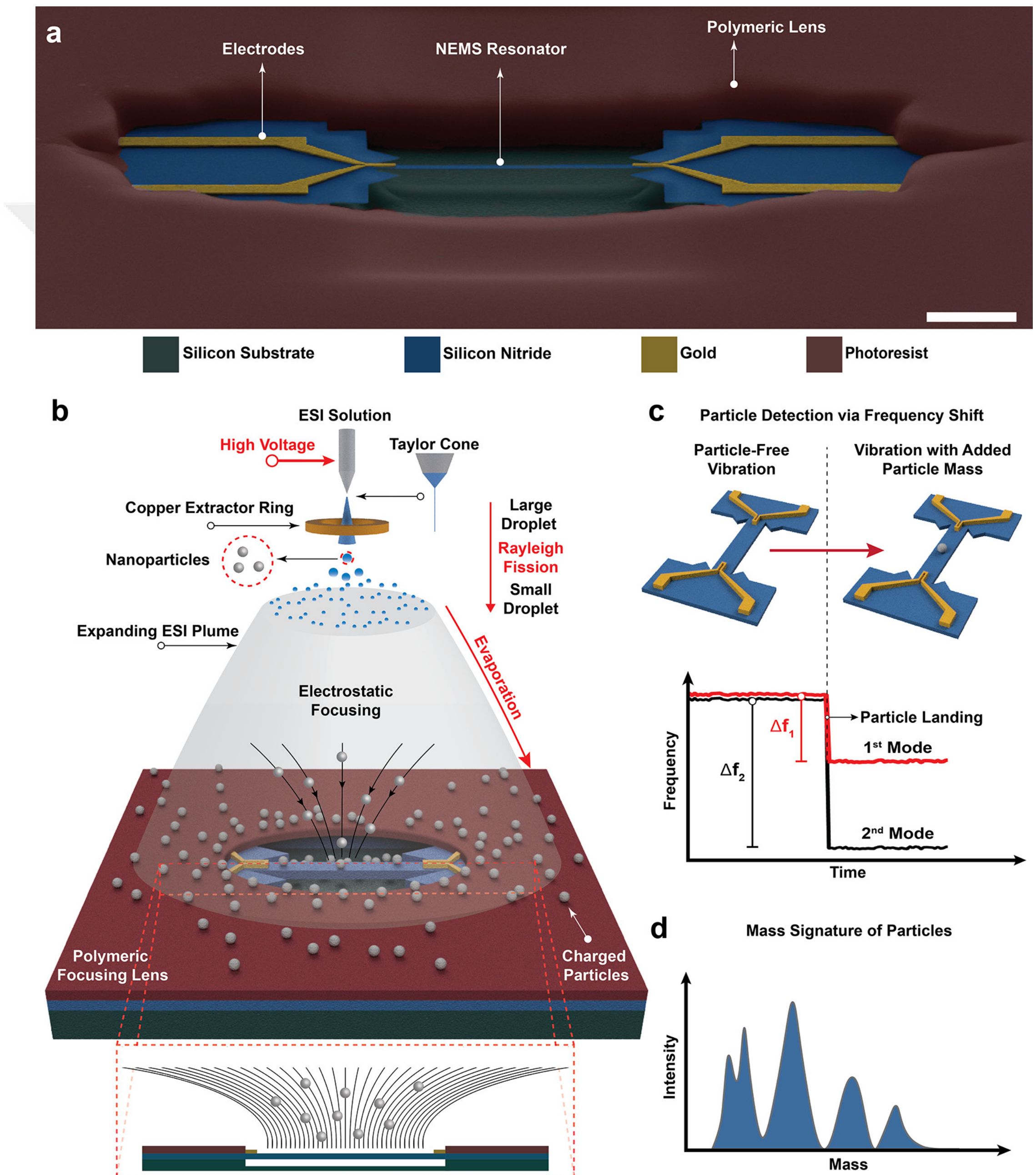

Figure C.1: Atmospheric Mass Spectrometry with NEMS, adapted from [14]

C.2 Atmospheric Single-Mode Mass Spectrometry with Paddle NEMS

In the mentioned methods, mostly doubly-clamped beams or cantilevers have been used [47,48]. However, when a uniform geometry is used for resonator geometry, the mass measurement of the analytes depends not only on their mass but also on where they land on the resonator. To resolve two unknowns, two knowns, namely the first and second mechanical modes of the resonator, have been used during the experiments [49]. This method is not preferable for two main reasons: employing two modes makes the experiments more complicated, and modes might diverge from their ideal expectations in ambient operations and cause uncertainties. To eliminate these, a different NEMS architecture was designed with a paddle region in the middle of a doubly-clamped beam to create a uniform mode shape at the first mechanical mode of the resonator. This uniform mode shape leads to position-independent mass sensing on the paddle region and the chance to use only the first mechanical mode of the resonator in the experiments [13,21]. I contributed as the <u>third author</u> to the publication of this work.

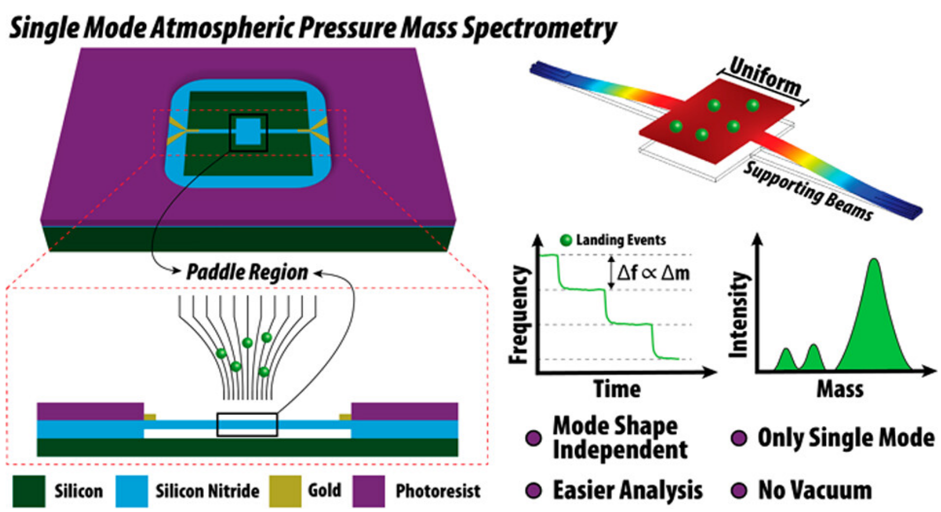

Figure C.2: Atmospheric Single-Mode Mass Spectrometry with Paddle NEMS, adapted from [21]